Effect of Flow-Direction-Dependent Dispersivity on Seawater Intrusion in Coastal Aquifers

Marwan Fahs, Behshad Koohbor, Qian Shao, Joanna Doummar, Husam M Baalousha, Clifford I Voss

AGU ADVANCING EARTH AND SPACE SCIENCE

Water Resources Research

RESEARCH ARTICLE
10.1029/2022WR032315

Effect of Flow-Direction-Dependent Dispersivity on Seawater Intrusion in Coastal Aquifers

Marwan Fahs[1], Behshad Koohbor[1], Qian Shao[2], Joanna Doummar[3], Husam M. Baalousha[4], and Clifford I. Voss[5]

[1]Institut Terre et Environnement de Strasbourg, Université de Strasbourg, CNRS, ENGEES, Strasbourg, France, [2]School of Civil Engineering, Wuhan University, Wuhan, PR China, [3]Department of Geology, American University of Beirut, Beirut, Lebanon, [4]Department of Geosciences, College of Petroleum Engineering and Geosciences, King Fahd University of Petroleum and Minerals (KFUPM), Dhahran, Saudi Arabia, [5]Water Resources Research Center, University of Hawaii, Honolulu, HI, USA

Key Points:

- Most existing modeling-based studies of seawater intrusion (SWI) assume constant dispersivities
- We investigate effect of flow-direction-dependent dispersivities on SWI based on the Henry problem and a typical coastal aquifer in Lebanon
- These results indicate the importance of employing an appropriate dispersion process representation when creating model-based SWI forecasts

Correspondence to:
Q. Shao,
qian.shao@whu.edu.cn

Citation:
Fahs, M., Koohbor, B., Shao, Q., Doummar, J., Baalousha, H. M., & Voss, C. I. (2022). Effect of flow-direction-dependent dispersivity on seawater intrusion in coastal aquifers. *Water Resources Research*, *58*, e2022WR032315. https://doi.org/10.1029/2022WR032315

Received 6 MAR 2022
Accepted 8 JUL 2022

Abstract Flow-direction-dependent (FDD) dispersivity in coastal aquifers (CAs) may strongly affect the inland extend of seawater intrusion (SWI) and the accompanying vertical salinity distribution. FDD dispersivity may predict greater inland intrusion of the saltwater wedge, but less vertical spreading of salinity than does the classical flow-direction-independent (FDI) dispersivity, the standard currently employed in most numerical CA models. Dispersion processes play a key role in the SWI process and directly affect CA pumped water quality. Constant FDI dispersivities may be inappropriate in representing mixing processes due to large differences between depth and horizontal salinity transport scales, and due to typical structured heterogeneities in aquifer fabrics. Comparison of FDI and FDD model forecasts for the classical Henry problem (HP) steady-state SWI, based on a new HP semianalytical solution with FDD and on a numerical FDI model modified to additionally represent FDD, highlights the theoretical types of differences implied by these alternative dispersivity assumptions and exactly how each parameter affects the solution. Large differences between FDI and FDD dispersivity forecasts of time-dependent SWI in large scale heterogeneous aquifers occur in a typical CA (Akkar CA, Lebanon). The FDD model forecasts that future salinities in pumping wells will exceed the potable water limit, whereas the FDI model greatly underestimates the historic inland intrusion of the saltwater wedge and forecasts no impact on future Akkar CA potable water supply. These results indicate the importance of employing the appropriate dispersion process representation when creating model-based SWI forecasts, especially for developing effective CA management strategies.

1. Introduction

1.1. Seawater Intrusion: Modeling Approaches

Numerical modeling has become an essential and popular tool for investigating seawater intrusion (SWI) in coastal aquifers (CAs; Werner et al., 2013). SWI models are helpful in practical studies for multiple purposes, such as the development of strategies for groundwater management in coastal areas (e.g., Hussain et al., 2019; van Engelen et al., 2019), the development of remediation, prevention, and monitoring techniques (e.g., Abdoulhalik & Ahmed, 2017; Bouzaglou et al., 2018; Chang et al., 2019; Graham et al., 2018; Karatzas & Dokou, 2015; Mehdizadeh et al., 2020; Strack et al., 2016; Zheng et al., 2020), and in predictive studies that consider climate change (Ketabchi et al., 2016) and/or anthropogenic stresses (e.g., Kalaoun et al., 2018).

Processes of SWI can be simulated using a sharp-interface model (SIM), which assumes immiscibility between freshwater and seawater. With this simplification, analytical solutions of the governing equations can be obtained based on the Ghyben-Herzberg relation (see Llopis-Albert et al., 2016, and references therein). The SIMs are used in practical applications because of their simplicity and low computational cost. However, it is well known that mixing between saltwater and freshwater plays an important role in controlling SWI, and in establishing the region of potable water because the typical potable limit for drinking water worldwide is ~1–2% seawater in pumped groundwater.

The sharp-interface approach is reasonably good for learning about and predicting the overall bulk movement response of the subsurface body of seawater. However, this approach is not appropriate for understanding and predicting the position of the 1–2% seawater isohyets that control the availability of a potable groundwater supply.

As this potability question is normally the main concern of water-supply managers, the sharp-interface approach is not appropriate for predicting the evolution of potable coastal groundwater supplies and for CA water-supply management.

The variable-density flow (VDF) model is more suitable for these purposes, as it can account for the impact of mixing processes when forecasting the subsurface boundary of potable water in a CA. It considers the mixing zone surrounding the freshwater-saltwater interface, which plays a crucial role in groundwater management in coastal areas (Lu & Luo, 2010). The mixing processes are represented by the diffusion-dispersion tensor in the salt transport equation (Abarca et al., 2007). VDF models are more computationally demanding than SIMs because they involve solving a nonlinear system of equations coupling flow and salt transport under conditions of variable fluid density.

1.2. The Henry Problem

The Henry problem (HP; Henry, 1964) is the most popular and first benchmark for SWI simulation based on the VDF model. It is a hypothetical benchmark for steady-state SWI that has been widely used as a surrogate in practical research to understand the physical processes of SWI. A review of the applications of the HP can be found in Fahs et al. (2018). In the original versions of the HP, an exaggerated single-valued diffusion coefficient was used to represent all mixing at the freshwater-seawater interface. This simplification was necessary to obtain a semianalytical (SA) solution (Dentz et al., 2006; Henry, 1964; Ségol, 1994; Simpson & Clement, 2004), but it is a limitation of the HP. While some mixing of freshwater and seawater in an aquifer is caused by molecular diffusion (i.e., pure mixing related to a concentration gradient), the constant diffusion coefficient employed in the original Henry SA solution is not representative of hydrodynamic dispersion processes.

A velocity-dependent dispersion tensor is usually used in the mass transport models to account for hydrodynamic dispersion (Abarca et al., 2007). Based on numerical simulations with the SUTRA code (Provost & Voss, 2019), Abarca et al. (2007) suggested a dispersive rather than diffusive HP, providing a new version of the problem that accounts for velocity-dependent dispersion and anisotropy. They showed that dispersion leads to isohyets similar to those observed in the field. Fahs et al. (2016) developed a new SA solution of the dispersive HP and studied the effect of transverse and longitudinal dispersion on several metrics of SWI. Fahs et al. (2018) also extended the SA solution to heterogeneous and anisotropic aquifers.

1.3. Representation of Dispersion

Realistic evaluation of the dispersive flux in porous media has received significant attention in the literature. Dispersion coefficients can be evaluated with a stochastic approach based on Monte Carlo simulations (de Dreuzy et al., 2012). Several studies evaluate the dispersion coefficient by performing pore scale simulations and an upscaling process (Gouze et al., 2021). Specific attention has been devoted to the evaluation of dispersion flux in problems involving density-driven flow in heterogeneous domains, where the velocity field has a complex structure (Dell'Oca et al., 2018; Nick et al., 2009). In the existing SA solutions of the HP as well as in some current numerical models of VDF (e.g., SEAWAT (Langevin et al., 2012), OpenGeoSys (Kolditz et al., 2012), FEFLOW (Diersch, 2014), and HydroGeoSphere (Graf & Therrien, 2005)), the velocity-dependent dispersion tensor relies on constant single-valued dispersivities to represent longitudinal and transverse dispersion processes. However, in several studies of contaminant transport in porous media, the dispersivities are shown to be dependent on the flow directions (e.g., Valdés-Parada et al., 2016).

One typical characteristic of CAs is that the domains are typically much larger horizontally than vertically. Horizontally, the domains can be several kilometers wide, whereas the vertical domain size is only tens of meters. Where the groundwater flow is horizontal, it likely encounters flow-field heterogeneities much larger than the thickness of the aquifer. Dispersivity values are related to the size of such heterogeneities; thus, longitudinal dispersivity for horizontally flowing water, over the distance from the recharge area to coastal wells or to the sea, is often much greater than the vertical size of the aquifer. Near the sea and below pumping wells, where the flow may become nearly vertical, the use of this high longitudinal dispersivity value would overestimate the vertical mixing process. When the flow is vertical, because of the small vertical spatial scale and smaller flow-field heterogeneities encountered by any vertical groundwater flow, the longitudinal dispersivity should be a fraction of the vertical extent of the aquifer, which is much smaller than the longitudinal dispersivity for horizontally

flowing water. This is one reason that a realistic representation of the dispersion processes in a multidimensional velocity field, such as in CAs, should consider the flow-direction dependence of the dispersivity parameters, and Reilly (1990) demonstrated this need for flow-direction-dependent (FDD) values of longitudinal dispersivity.

Another reason for needing FDD representation of dispersivities is discussed by Voss (1984). Where there is an anisotropic spatial distribution of heterogeneities in subsurface aquifer materials that affects the ease of groundwater flow, the same amount of dispersion would not occur for flow in all directions, even when the magnitude of the mean flow velocity, v, is the same in each direction. For example, in a layered aquifer, the amount of dispersion would not necessarily be the same for flow parallel to the layers and for flow perpendicular to the layers.

The isotropic-media dispersion representation, described above and used by most numerical codes that solve the SWI problem, does not account for the above-described possibilities, because its basic parameters, the dispersion coefficients (α_L and α_T), are independent of flow direction. Thus, the widely used standard description of dispersion with flow-direction-independent (FDI) dispersivities relies on an "isotropic media model" that is not a good descriptor of dispersion in typical geologic formations, nor is it an appropriate description of dispersion in most aquifers due to the differences in horizontal and vertical scale of heterogeneities encountered by horizontally and vertically flowing groundwater.

Voss (1984) hypothesized an ad-hoc description of dispersion for anisotropic media that allows key aspects of expected dispersion behavior in anisotropic geologic fabrics to be represented. The anisotropic media form of longitudinal dispersivity dependence on the direction of flow relative to the principal permeability directions, described by Voss (1984), is similar to that found by a stochastic analysis of macrodispersion in a transversely isotropic medium (Gelhar & Axness, 1983). Initially, the description provided was only for direction dependence of longitudinal dispersivity in two spatial dimensions, but the "anisotropic media model" was later extended to include flow-direction dependence of transverse dispersivity and was generalized to three spatial dimensions (Voss & Provost, 2002). Although this hypothetical description is neither completely general nor rigorous, it provides a practical means of describing dispersion in anisotropic media and in aquifers with contrasting horizontal and vertical scales.

Upon introducing the "anisotropic media model," Voss (1984) provided some practical considerations for applying dispersion representations that are applied to SWI problems in the current work. When there is a lack of direct measurements of longitudinal dispersivities, the values employed in an analysis of SWI may either be on the order of the size of the largest hydrogeologic or flow inhomogeneities along the transport reach, or be the distance between inhomogeneities, whichever is the greater value. Should the longitudinal dispersivity, estimated on the basis of the size of inhomogeneities or distance between them, be greater than about one-tenth of the longest transport reach, then the meaningful use of a constant-dispersivity dispersion model could be questioned, as the effective longitudinal dispersivity would increase in value as the groundwater travel distance increases. In such a case, the ideal action to take would be to more explicitly define the field distribution of velocity by taking into account the actual geometry of the most important inhomogeneities. This would correctly account for most of the transport that takes place as being advective in nature, with much smaller contributions of the approximate representation of the dispersive process. Given a better-defined velocity field, and in the absence of other data, dispersivity should then be chosen based on the largest postulated inhomogeneities met along a given average stream tube. The size and distribution of inhomogeneities not explicitly taken into account by the average flow field may be postulated based on the best available knowledge of local geologic structure in a CA.

Voss (1984) also considered practical approaches to evaluate the impact of transverse dispersivity on solute transport, indicating that transverse dispersivity values are typically even less well known for field problems than longitudinal dispersivity. Transverse dispersivity values used in quantitative analyses and groundwater modeling are typically between one-tenth and one-third of longitudinal dispersivity. However, in systems with anisotropic permeability, transverse dispersivity may be less than one-hundredth of longitudinal dispersivity for flows along the maximum permeability direction (Gelhar & Axness, 1983). Should simulated transport in a particular situation, such as SWI, be sensitive to the value of transverse dispersivity, further data collection is necessary and the transport model predictions must be interpreted with great care and caution.

Depending on the particular geometry of layers or inhomogeneities causing the permeability anisotropy, the longitudinal dispersivity for flow in the minimum permeability direction, α_{Lmin}, may be either greater or smaller than those for flow in the middle and maximum permeability directions, α_{Lmid} and α_{Lmax}. However, the use of the

anisotropic-media dispersion model is advised only when required by field data and for theoretical analyses such as the present one. The additional longitudinal dispersion parameters are not intended for general application without evaluation of their applicability in each particular case.

Another use of the ad-hoc FDD dispersivities model is in the case of 2D cross-sectional or 3D simulation wherein the lateral extent of the system is much greater than the vertical extent as most often occurs in CAs that experience SWI. In this case, lateral flow and transport may be affected by the larger heterogeneities that exist in the larger lateral direction, and vertical flow and transport may be affected by smaller heterogeneities that exist in the much smaller vertical direction. In this common situation, it usually makes sense to employ the ad-hoc FDD dispersivities model and to assign different longitudinal and transverse dispersivities for lateral and vertical flow.

1.4. Goals of Present Analyses

The ad-hoc FDD dispersivity models for longitudinal and transverse dispersivity in anisotropic media presented by Voss (1984) and Voss and Provost (2002) allow for simulation experiments with two or three principal longitudinal and transverse dispersivity values. Studying the impact of FDD longitudinal and transverse dispersivity model on SWI and comparison with results from the commonly used FDI dispersivity model is the focus of the current analysis.

This work aims to provide some understanding of the effect of FDD dispersivities on SWI. Thus, a new SA solution of the HP is developed that considers FDD dispersivities. Also, an in-house finite element code is modified to include FDD dispersivities. The new code is validated by comparison against the newly developed SA solution and results obtained from the SUTRA code (version 2.2, Voss & Provost, 2010). Based on the HP, three models based on FDI and FDD dispersivities are compared. The HP is also used to perform a global sensitivity analysis to evaluate the effect of model parameters on SWI metrics. The newly developed code is then used to simulate SWI in the Akkar CA in Lebanon. It was used to predict the extent of SWI under climate change and anthropogenic stresses in the Akkar CA and results are compared for FDI and FDD dispersivities. Results evaluate and compare the effect of FDD versus FDI dispersivities on SWI at field scale, in heterogeneous domains, and under dynamic and pumping conditions.

2. Methods

2.1. Governing Equations

The governing equations of the FDD model are presented in this section. Fluid flow in saturated porous media is governed by Darcy's law

$$\mathbf{q} = -\frac{\rho_0 \boldsymbol{k} g}{\mu}\left(\nabla h + \frac{\rho - \rho_0}{\rho_0}\nabla z\right) \tag{1}$$

where $\mathbf{q}$ is the Darcy velocity $[L\ T^{-1}]$, ρ_0 is the freshwater density $[M\ L^{-3}]$, g is the gravitational acceleration $[L\ T^{-2}]$, $\boldsymbol{k}$ is the diagonal intrinsic permeability tensor of the porous medium $\left[L^2\right]$, μ is the viscosity of the fluid $[M\ L^{-1}\ T^{-1}]$, h is the equivalent freshwater head $[L]$, ρ is the density of the fluid $[M\ L^{-3}]$, and z is the upward vertical direction $[-]$. The viscosity is assumed to be constant.

The mass balance of the fluid, under the Oberbeck-Boussinesq approximation, is given by (Guevara Morel et al., 2015)

$$S_s \frac{\partial h}{\partial t} + \nabla . q = f \tag{2}$$

where S_s is the specific storage coefficient $\left[L^{-1}\right]$ and f is the sink/source term $\left[T^{-1}\right]$. The solute mass balance is given by an advection-dispersion equation as follows:

$$\varepsilon \frac{\partial c}{\partial t} + \mathbf{q}\nabla c - \nabla \cdot (\varepsilon D_m \mathbf{I} + \mathbf{D})\nabla c = 0 \tag{3}$$

where c is the dimensionless solute concentration $[-]$ (salt concentration divided by sea salinity), ϵ is the porosity of the porous medium $[-]$, D_m is the molecular diffusion coefficient $[L^2\,T^{-1}]$, I is the identity matrix and $\mathbf{D}$ is the dispersion tensor $[L^2\,T^{-1}]$ defined by (Abarca et al., 2007)

$$\mathbf{D} = (\alpha_L - \alpha_T)\,\frac{\mathbf{q}\times\mathbf{q}}{|\mathbf{q}|} + \alpha_T|\mathbf{q}|\mathbf{I} \tag{4}$$

where $\alpha_L\,[L]$ and $\alpha_T\,[L]$ are, respectively, longitudinal and transverse dispersivities.

The dispersion coefficients can be predicted using the homogenization approach as in Held et al. (2005) and Dentz et al. (2020). In this work, we use FDD dispersivities. For a two-dimensional spatial system, these coefficients are defined as follows (Voss & Provost, 2002):

$$\alpha_L = \frac{\alpha_L^{\max}\alpha_L^{\min}}{\alpha_L^{\min}\cos^2\theta_{kv} + \alpha_L^{\max}\sin^2\theta_{kv}} \tag{5}$$

$$\alpha_T = \frac{\alpha_T^{\max}\alpha_T^{\min}}{\alpha_T^{\min}\sin^2\theta_{kv} + \alpha_T^{\max}\cos^2\theta_{kv}} \tag{6}$$

where $\alpha_L^{\max}$ (resp. $\alpha_T^{\max}$) and $\alpha_L^{\max}$ (resp. $\alpha_T^{\min}$) are the longitudinal (resp. transverse) dispersivities in the maximum and minimum directions of permeability (or hydraulic conductivity) and θ_{kv} is the counterclockwise angle between the direction of maximum permeability and the fluid velocity direction.

Rewriting $\cos\theta_{kv} = \frac{q_x}{|\mathbf{q}|}$ and $\sin\theta_{kv} = \frac{q_z}{|\mathbf{q}|}$, leads to a representation in terms of fluid velocity components

$$\alpha_L = \frac{|\mathbf{q}|^2\alpha_L^{\max}\alpha_L^{\min}}{\alpha_L^{\min}q_x{}^2 + \alpha_L^{\max}q_z{}^2} \tag{7}$$

$$\alpha_T = \frac{|\mathbf{q}|^2\alpha_T^{\min}\alpha_T^{\max}}{\alpha_T^{\min}q_z{}^2 + \alpha_T^{\max}q_x{}^2} \tag{8}$$

The flow (Equation 3) and transport (Equation 4) equations are coupled via the linear mixture density equation:

$$\rho = \rho_0 + (\rho_1 - \rho_0)\,c \tag{9}$$

where ρ_1 is the seawater density $[M\,L^{-3}]$.

In this analysis, in order to allow direct comparison of results with the constant dispersion model, the average values of the FDD longitudinal and transverse dispersivities ($\overline{\alpha_L}$ and $\overline{\alpha_T}$) and their ranges of variability (l_L and l_T) are considered as primary parameters instead of the maximum and minimum values. In this case, the FDI model with constant dispersivities corresponds to $l_L = l_T = 0$. These parameters are defined as follows:

$$\begin{aligned}
\overline{\alpha_L} &= \frac{\alpha_L^{\min} + \alpha_L^{\max}}{2}\\
\overline{\alpha_T} &= \frac{\alpha_T^{\min} + \alpha_T^{\max}}{2}\\
l_L &= \alpha_L^{\max} - \alpha_L^{\min}\\
l_T &= \alpha_T^{\max} - \alpha_T^{\min}
\end{aligned} \tag{10}$$

Relations in Equation 10 can be rearranged as follows:

$$\begin{aligned}
\alpha_L^{\min} &= \overline{\alpha_L} - \frac{l_L}{2}\\
\alpha_L^{\max} &= \overline{\alpha_L} + \frac{l_L}{2}\\
\alpha_T^{\min} &= \overline{\alpha_T} - \frac{l_T}{2}\\
\alpha_T^{\max} &= \overline{\alpha_T} + \frac{l_T}{2}
\end{aligned} \tag{11}$$

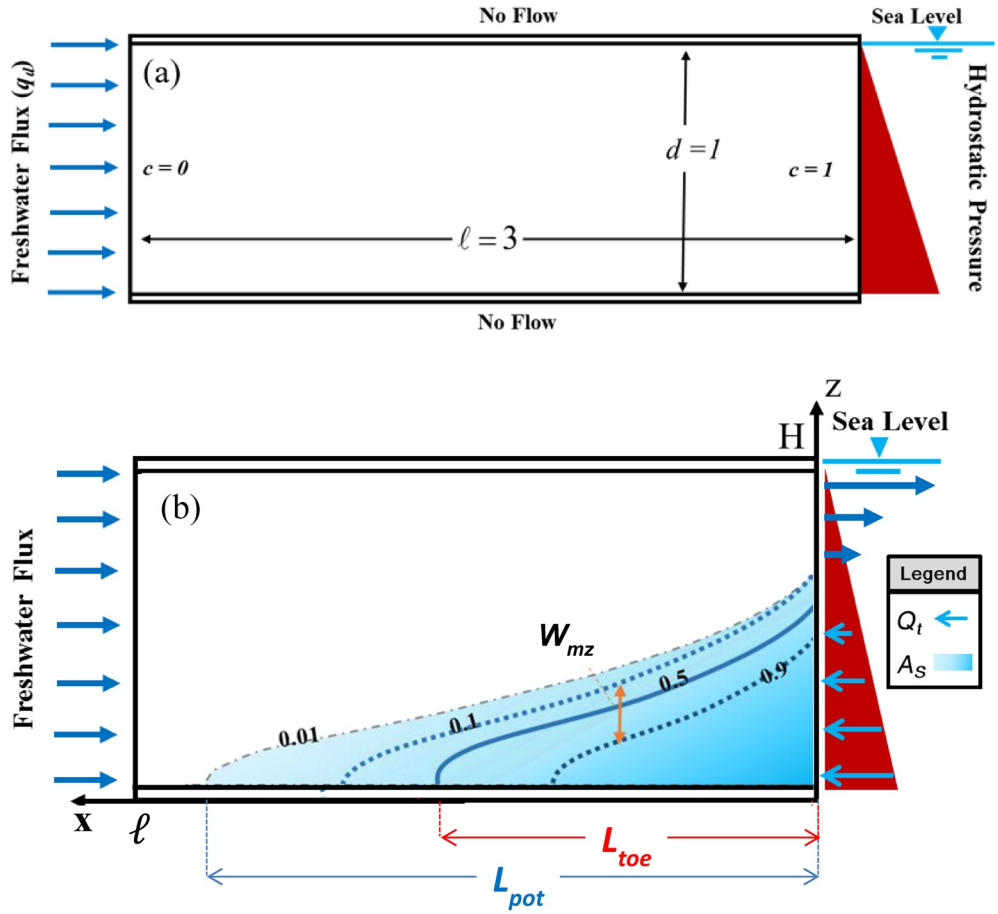

Figure 1. Schematic representation of (a) the Henry problem (HP) and associated boundary conditions for the new semianalytical (SA) solution and (b) the seawater intrusion (SWI) metrics. W_{mz} is the vertical distance between the 0.1 and 0.9 isohyets. The average of W_{mz} on the x-axis between $X = 0.2L_{toe}$ to $X = 0.8L_{toe}$ is defined as the width of the mixing zone. Q_t is the total dimensionless flux of saltwater entering the aquifer and A_s is the dimensionless salinized area.

2.2. HP and SA Solution

The domain of the HP consists of a rectangle, in vertical cross-section, with a depth (d) and a length (ℓ). The boundary conditions are given by

$$x = 0 \begin{cases} c = 1 \\ h = \rho_s(H - z)/\rho_0 \end{cases}$$
$$x = \ell \begin{cases} c = 0 \\ q_x = q_d \end{cases} \quad (12)$$
$$y = 0, H \begin{cases} \partial c/\partial z = 0 \\ q_z = 0 \end{cases}$$

The aquifer concentration along the sea boundary is held at $c = 1$. Note that this is a simplification needed to obtain an analytical solution. It is not the natural boundary condition for this location, which instead would set the concentration of discharging groundwater to its ambient concentration (calculated by the model) and would set the concentration of inflowing water to be that of seawater ($c = 1$). Figure 1a describes the HP domain for developing the SA solution.

Stream function theory is used to obtain the SA solution (presented in Appendix B). The nondimensional analysis shows that the flow and transport processes are governed by seven parameters defined as follows:

$$r_k = \frac{k_z}{k_x} \tag{13}$$

$$NG = \frac{k_z g\,(\rho_1 - \rho_0)}{\mu q_d} \tag{14}$$

$$b_m = \frac{\varepsilon D_m}{q_d} \tag{15}$$

$$\overline{A_L} = \frac{\overline{\alpha_L}}{d} \tag{16}$$

$$\overline{A_T} = \frac{\overline{\alpha_T}}{d} \tag{17}$$

$$L_L = \frac{l_L}{d} \tag{18}$$

$$L_T = \frac{l_T}{d} \tag{19}$$

where $k_x\left[L^2\right]$ and $k_z\left[L^2\right]$ are the principle permeabilities in the x and z directions.

The SA solution is obtained by expanding the concentration and the stream function in appropriate Fourier series (see Appendix B). A Galerkin treatment is then applied by using the Fourier modes as trial functions. The Galerkin integrals are evaluated analytically except for the dispersion terms, which are evaluated numerically using an adaptive higher-order integration scheme. This leads to a final spectral system consisting of nonlinear algebraic equations that are solved using the Powell algorithm of the IMSL library. This allows for expressing the concentration and the stream function (and in consequence the velocity field) as functions of space coordinates.

2.3. A Revised Numerical Code: Modification of TRACES

TRACES (Transport of RadioACtive Elements in Subsurface) is an in-house research simulator (at Université de Strasbourg) based on advanced numerical schemes (Hoteit et al., 2004). It can simulate 2D or 3D flow, mass, and heat transport in porous media. Another version of this simulator, allowing for VDF was developed by Younes et al. (2009) and Shao et al. (2018). TRACES is based on the mixed hybrid finite element method for the discretization of the flow equation and a combination of a discontinuous Galerkin finite element method and multiple-flux approximation method for the discretization of advection and dispersion transport operators, respectively. Time integration is performed using an adaptive variable order technique via the method of lines. The numerical methods used in TRACES are described in Younes et al. (2009). Dispersion in TRACES was originally based on constant FDI dispersivities. An enhanced 2D version of this code was developed for the current study by including FDD dispersivities, as in Equations 7 and 8.

2.4. Metrics for SWI and Global Sensitivity Analysis

Using the new SA solution of the HP, a global sensitivity analysis was conducted to understand the effect of the parameters controlling dispersion variability ($\overline{A_L}$, $\overline{A_T}$, L_L, and L_T, Equations 16–19) on several metrics characterizing SWI. To assess SWI, the following metrics are used (see Figure 1b):

- Dimensionless length of the saltwater toe (L_{toe}): The horizontal distance from the sea boundary to the 0.5 isohyet on the bottom surface of the aquifer divided by the aquifer depth (d).
- Dimensionless length of the potable water threshold (L_{pot}): The horizontal distance from the sea boundary to the 0.01 isohyet on the bottom surface of the aquifer divided by the aquifer depth (d).
- Dimensionless average vertical width of the mixing zone (W_{mz}): The average vertical distance between the 0.1 and 0.9 isohyets, between $X = 0.2L_{toe}$ to $X = 0.8L_{toe}$, divided by the aquifer depth (d). The mixing zone considered here is limited to be between $X = 0.2L_{toe}$ and $X = 0.8L_{toe}$ to avoid boundary effects and to ensure

Table 1
Nondimensional Parameters Used for the Henry Problem (HP) in the Verification Test Case and in Sensitivity Analysis

	Verification test case	Values for sensitivity analysis
r_k	1	0.66
NG	3.79	3.79
b_m	5×10^{-4}	5×10^{-4}
$\xi(=\ell/d)$	3	3
$\overline{A_L}$	0.055	[0.005, 0.5]
L_L	0.09	[0, 0.5]
$\overline{A_T}$	0.055	[0.001, 0.1]
L_T	0.09	[0, 0.2]

the existence of both isohyets 0.1 and 0.9 within the $0.2L_{toe}$ to $0.8L_{toe}$ range (Abarca et al., 2007).

- Total dimensionless flux of saltwater entering the aquifer (Q_t): The flux of saltwater entering the domain by advection, diffusion, and dispersion. Dimensionless flux is calculated using the dimensionless concentration, velocity, and diffusion coefficients given in Appendix B. The diffusive and dispersive fluxes are calculated over the entire sea boundary while the mass flux related to advection is calculated along the inland flow zone of the seaside boundary (see Fahs et al., 2016).
- The dimensionless salinized area (A_s): Sum of the area of elements having a salt concentration of >0.01 (blue area in Figure 1b) divided by the area of the domain. The dimensionless area of the zone of freshwater (i.e., concentration <0.01) is also used in the discussion. This area, denoted by A_F, is calculated as the difference between the domain's total dimensionless area (i.e., 1) and A_s, $A_F = 1 - A_s$.

The global sensitivity analysis, described in Appendix C, is performed using the Bayesian sparse Polynomial Chaos Expansion (PCE) approach that was proposed by Shao et al. (2017). This is a metamodeling-based method, which constructs a surrogate model upon multivariate orthogonal polynomials to reproduce the input-output relationship of the original physical model. Then the Sobol' indices (SIs), adopted as the sensitivity metrics, can be computed analytically from the PCE coefficients (Fajraoui et al., 2017).

3. Results for the HP

3.1. Verification of the SA Solution Against TRACES and SUTRA: Effect of the Sea Boundary Conditions

The correctness of both the new SA code and TRACES was verified via a reference solution that can be used for code validation. The nondimensional and physical parameters of the verification case are given in Tables 1 and 2, respectively. For the current test case, the same values of average and variability are employed for both transverse and longitudinal dispersivities. This is atypical of a realistic setting, but it is used here to allow more-direct understanding of the spatial distribution of the transverse dispersive flux. The SA solution is obtained using 4,725 Fourier modes. With TRACES, the mesh-independent solution is obtained using a grid consisting of 12,000 triangular elements. The main (0.01, 0.5, and 0.99) isohyets are plotted in Figure 2a in which the numerical and analytical isohyets are indistinguishable from each other, indicating an excellent match. Furthermore, the SWI metrics evaluated numerically and analytically are in excellent agreement ($L_{toe} = 1.33$, $L_{pot} = 1.45$, $W_{mz} = 0.27$, $Q_t = 1.12$, and $A_s = 0.85$). Digitized isohyets and numerical metrics are available in Appendix D.

In Figure 2b, the SA solution is compared with results from the SUTRA code (with a 384×128 mesh of rectangular finite elements). SUTRA simulations are performed with natural sea boundary conditions (not a fixed value of concentration at the vertical sea boundary). Where the water enters the boundary, it has seawater concentration and where it discharges from the boundary it has the ambient concentration of the groundwater (Voss & Souza, 1987; Yang et al., 2013). In contrast, a specified constant concentration is imposed along the sea boundary in the SA solution as a mathematical necessity for obtaining an analytical solution, as discussed earlier. The SA and SUTRA solutions are in excellent agreement, except near the sea boundary (Figure 2b), where these different boundary conditions necessarily cause a discrepancy between the solutions. The TRACES code was run with natural sea boundary conditions and the results of TRACES and SUTRA are also in good agreement (Figure 2b) even near the sea boundary.

3.2. Implications of FDD Dispersivities for Salinity Transport

To understand the mixing processes within the mixing zone, the spatial maps of A_L and A_T are plotted in Figures 3a and 3c together with the 0.01, 0.5, and 0.99 isohyets and the velocity field. In Figure 3b (and

Table 2
Physical and Nondimensional Parameters for the Verification Test Case, the Sensitivity Analysis, and the Case Study in Lebanon

	Verification test case (HP)	Case study in Lebanon
Freshwater density ρ_0 $(\mathrm{kg \cdot m^{-3}})$		1, 000
Seawater density ρ_1 $(\mathrm{kg \cdot m^{-3}})$		1, 025
Seawater salinity (TDS/(fluid volume)) C_s $(\mathrm{kg \cdot m^{-3}})$or $(\mathrm{g \cdot L^{-1}})$		39
Gravity g $(\mathrm{m \cdot s^{-2}})$		9.81
Viscosity μ $(\mathrm{kg \cdot m^{-1} \cdot s^{-1}})$		10^{-3}
Aquifer permeability k_z $(\mathrm{m^2})$	1.02×10^{-9}	Zone 1: 1.01×10^{-12}; Zone 2: 8.15×10^{-12}; Zone 3: 5.09×10^{-13}; Zone 4: 1.01×10^{-14}; Zone 5: 3.05×10^{-13}; Zone 6: 1.01×10^{-12}; Sediment: 1.01×10^{-14}
Anisotropy ratio r_k $(= k_z/k_x)$	1	0.1
Porosity ϵ	0.35	Zones 1, 2, 3: 0.3
		Zones 4, 5, 6: 0.2
Storage coefficient S_s $(\mathrm{m^{-1}})$	0	Zones 1, 2, 3: 5×10^{-4}
		Zones 4, 5, 6: 5×10^{-6}
Domain dimensions (m)	$\ell = 3$ and $d = 1$	See Figure 8
Molecular diffusion D_m $(\mathrm{m^2 \cdot s^{-1}})$	9.43×10^{-8}	1.0×10^{-9}
Avg. longitudinal dispersivity $(\overline{\alpha_L})$ (m)	0.055	5
Range of variability l_L (m)	0.09	8
$\alpha_T^{\min}$(m); $\alpha_L^{\max}$	0.01; 0.1	1; 9
Avg. transverse dispersivity $(\overline{\alpha_T})$ (m)	0.055	0.5
Range of variability l_T (m)	0.09	0.8
$\alpha_T^{\min}$; $\alpha_T^{\max}$	0.01; 0.1	0.1; 0.9
Regional flow/unit width q_d $(\mathrm{m^2 \cdot s^{-1}})$	6.6×10^{-5}	6.4×10^{-9}

Figure 3d), the absolute value of the longitudinal (and transverse) dispersion flux, calculated by projecting the total dispersive flux in the direction parallel to (and orthogonal to) the velocity is plotted together with the velocity flow directions.

Figure 3a shows that the maximum value of A_L occurs, as expected, in the zone where the velocity is horizontal. Figure 3b shows that longitudinal dispersion flux is insignificant outside the mixing zone, where solute concentrations are nearly constant. Within the mixing zone, A_L exhibits its maximum values in the deepest part of the transition zone, where the highest horizontal concentration gradients occur. Around the 0.5 isohyet, despite the concentration gradient, a narrow zone with insignificant longitudinal dispersion flux appears (Figure 3b), and in this zone, A_L is insignificant because velocities are vertical (Figure 3a). To further understand the effect of variable dispersivities on the dispersion fluxes, the absolute values of the longitudinal and transverse dispersion fluxes with the FDI dispersivities model are plotted in Figure 4. Figure 4a shows that, as for FDD dispersivities, a zone of low longitudinal dispersion flux is observed around the 0.5 isohyet with the FDI dispersivities. This indicates that this zone of low longitudinal dispersive flux is not related to the variability of the dispersion coefficients, but rather to the concentration gradient. However, different patterns occur in the results for FDD and FDI dispersivities in other parts of the mixing zone. With FDI dispersivities, continuous and uniform zones of high longitudinal dispersive flux are observed in the transition zones between the 0.5 and highest and lowest isohyets, respectively (i.e., 0.5–0.1 and 0.5–0.9). In contrast, these zones are not continuous with the FDD dispersivities. The nonuniform distribution of the longitudinal dispersive flux in this zone is related to the dependence of the longitudinal dispersion coefficient on the flow direction. The flow direction is highly variable in this zone due to the confluence of freshwater and saltwater flows.

The transverse dispersivity is small (i.e., between 0.01 and 0.02) everywhere in the domain, except in the midtransition-zone region, just mentioned, where the vertical component of velocity dominates (Figure 3c).

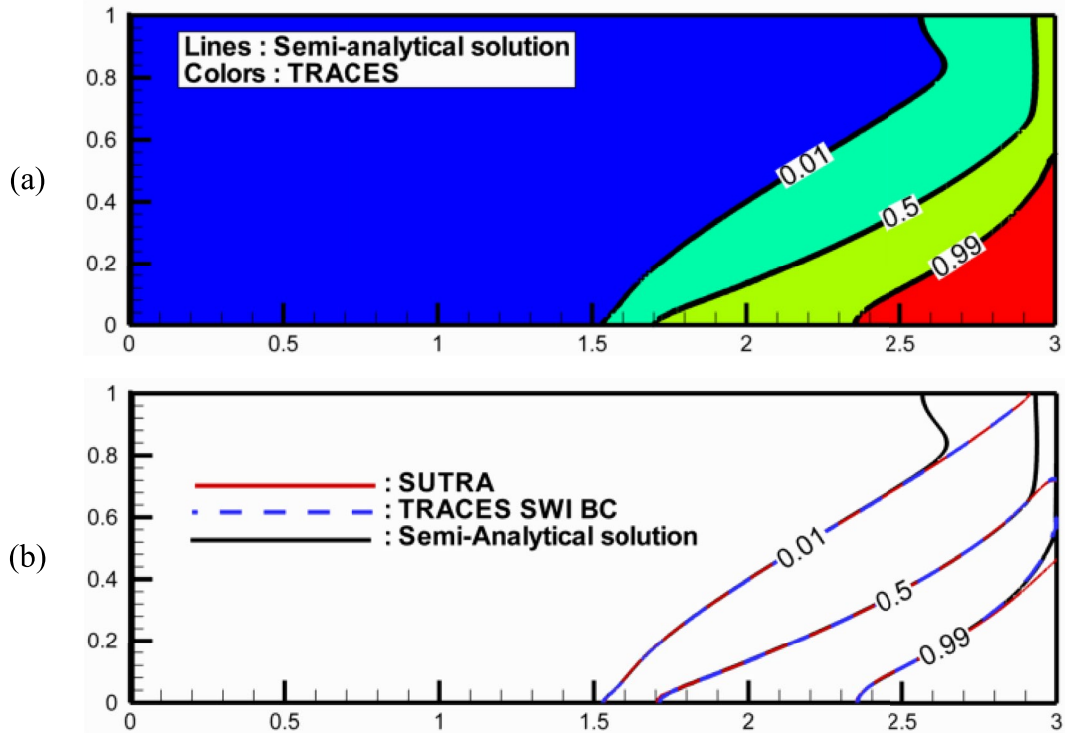

Figure 2. Main isohyets for the Henry problem (HP; verification test case): (a) comparison between the semianalytical (SA) solution and the in-house code TRACES and (b) comparison between SUTRA, TRACES with natural sea boundary conditions and the SA solution.

Complementary patterns can be observed in the spatial distributions of A_L and A_T. The zone of highest A_T, located around the 0.5 isohyet, is similar to the zone of lowest A_L. The transverse dispersive flux is significant in this zone (Figure 3d). Figure 4b shows that the spatial distribution of transverse dispersive flux with FDD and FDI dispersivities has the same patterns. However, it is clear that the model with FDI dispersivities predicts much greater transverse dispersive flux within the mixing zone than does the FDD representation.

3.3. Comparison Between FDD and FDI Representations

The model based on FDD dispersivities is also compared with the standard FDI model. As discussed in Section 4, 250 HP simulations were performed with different sets of parameters in order to construct the PCE metamodels, used in the sensitivity analysis. The ranges of the variability of the parameters are given in Table 1. Among this set of 250 simulations, the highest discrepancy between these models is observed with $\overline{A_L} = 0.25$, $L_L = 0.5$, $\overline{A_T} = 0.05$, and $L_T = 0.1$. For the FDI model, the dispersivities are considered to be constant by using the same average values for $\overline{A_L}$ and $\overline{A_T}$ as for the FDD model, but with zero values for L_L and L_T.

The isohyets obtained with the two HP models having the highest discrepancy are compared in Figure 5. This figure shows significant differences between the shapes of the isohyets. The FDI model predicts less inland intrusion of the saltwater wedge near the bottom of the aquifer, but much greater intrusion of saltwater to the shallower portion of the aquifer in the vicinity of the sea boundary. The FDD model leads to larger L_{toe}, L_{pot}, and A_s, than the FDI model. For these metrics, the discrepancies (absolute difference) between the models are calculated to be about 1, 0.47, and 0.66, respectively. Smaller W_{mz} and Q_t are obtained with the FDD model, with discrepancies of about 0.74 and 0.27, respectively. This corresponds to relative discrepancies of about 44.2%, 19.4%, 46.3%, 284%, and 490% for L_{toe}, L_{pot}, A_s, W_{mz}, and Q_t, respectively. The results show that, even when the same average dispersivities are used in both FDI and FDD models, neglecting the flow-direction dependency of the dispersiv-

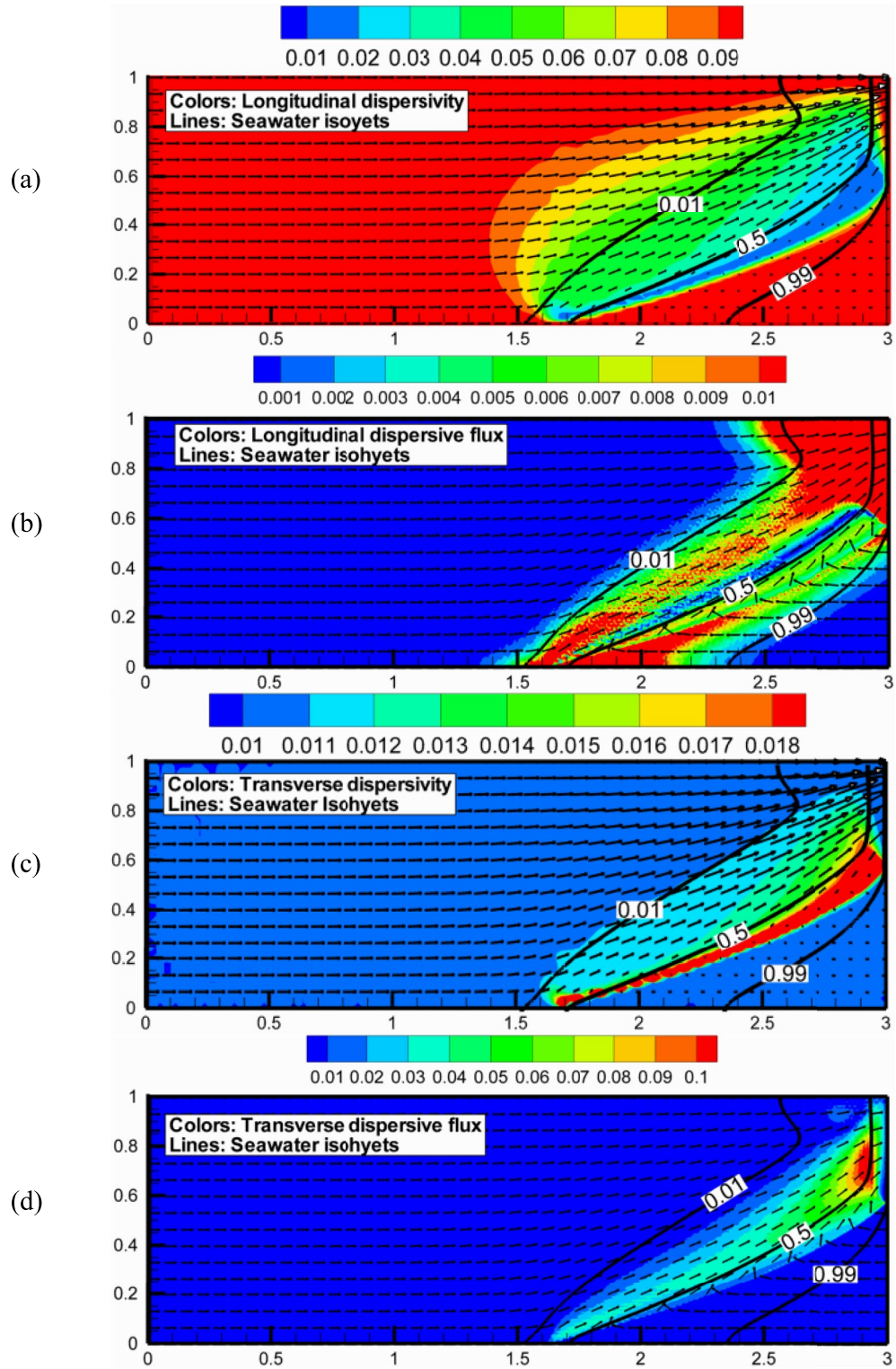

Figure 3. Spatial distributions of the dispersion coefficients and dispersive flux with flow-direction-dependent (FDD) dispersivities: (a) and (c) maps of the FDD dispersivities (A_L and A_T, respectively), with the isohyets 0.01, 0.5, and 0.99 and the velocity field, (b) absolute value of the longitudinal dispersive flux calculated as the projection of the dispersive flux on the direction parallel to the velocity, and (d) absolute value of the transverse dispersive flux calculated as the projection of the dispersive flux on the direction orthogonal to the velocity. The velocity directions (displayed with uniform line length) and isohyets (0.01, 0.5, and 0.99) are shown in (b) and (d).

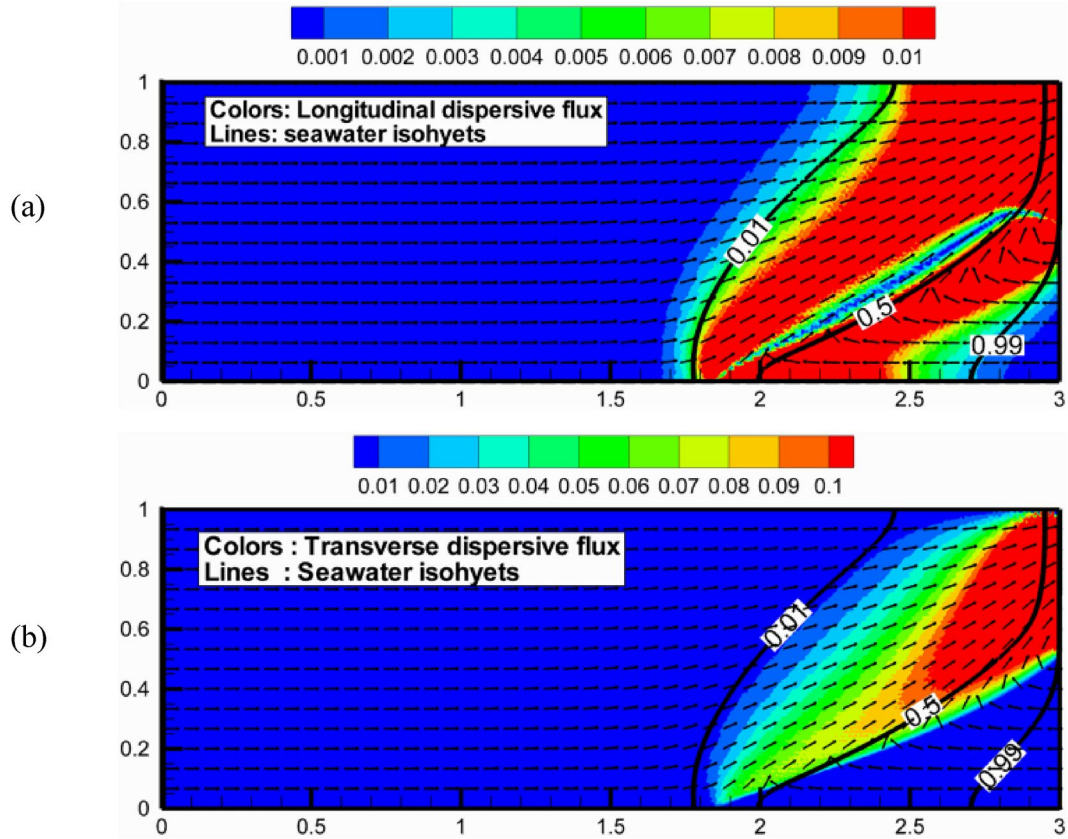

Figure 4. Dispersive fluxes with flow-direction-independent (FDI) dispersivities: (a) absolute value of the longitudinal dispersive flux calculated as the projection of the dispersive flux on the direction parallel to the velocity, and (b) absolute value of the transverse dispersive flux calculated as the projection of the dispersive flux on the direction orthogonal to the velocity.

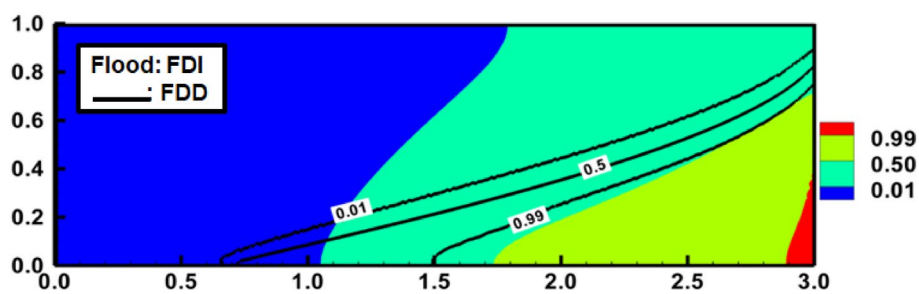

Figure 5. Henry problem (HP) comparison between isohyets obtained with same average dispersivity for flow-direction-dependent (FDD) dispersivity and for flow-direction-independent (FDI) dispersivity models. For both models: $\overline{A_L} = 0.25$, $\overline{A_T} = 0.05$. For FDD model: $L_L = 0.5$, $L_T = 0.1$. For FDI model: $L_L = L_T = 0$. Zero values of dispersivities are replaced by 0.001.

ities can significantly underestimate the toe of the saltwater wedge and can overestimate the total saltwater flux to the aquifer.

4. Influence of the FDD Dispersivities: Sensitivity of the SWI Metrics to $\overline{A_L}$, L_L, $\overline{A_T}$, and L_T

To investigate the effects of FDD dispersivities on SWI, a global sensitivity analysis for the anisotropic HP is performed. The natural sea boundary condition is used (Voss & Souza, 1987; Yang et al., 2013). All parameters of the HP are constant except $\overline{A_L}$, L_L, $\overline{A_T}$, and L_T which are considered to be uniformly distributed over their range of variations given in Table 1. These values are inspired by Abarca et al. (2007) and they are physically plausible. A training data set with 250 simulations is used to construct the PCE metamodels. The PCEs are validated using an independent set of 30 sample points obtained via an optimized Latin hypercube sampling strategy. The validation results are not presented here for the sake of brevity.

Figure 6 shows the total SIs (S_i^T) for the SWI metrics. For L_{toe} (Figure 6a), the most significant parameter is $\overline{A_T}$, the average magnitude of A_T. The sensitivity of L_{toe} to L_T is ranked second, indicating that the variability of the transverse dispersivity with flow direction can have a significant impact on the inland location of the toe of the saltwater wedge.

As expected, the width of the mixing zone is mainly controlled by $\overline{A_T}$ and $\overline{L_T}$, which are general controls on total mixing (Figure 6b). As occurs for L_{toe}, the variability of the transverse dispersivity with flow, L_T, has a significant impact on W_{mz}.

The evaluation of Q_t is adapted to deal with the natural sea boundary conditions. Only flux entering the domain is considered in Q_t. Again, $\overline{A_T}$ and L_T are the most important parameters (Figure 6c); however, the total salt flux (Q_t) is sensitive to all dispersion parameters.

Based on the SIs, the sensitivity of the salinity distribution to the FDD dispersivities is investigated. The spatial maps of SIs and standard deviation are not shown for sake of brevity. The results confirm that $\overline{A_T}$ is the most important parameter affecting the salinity distribution, followed by L_T.

The freshwater area (A_F) and, accordingly, the area of the saltwater wedge are mainly controlled by $\overline{A_T}$ and L_T. These measures are relatively sensitive to $\overline{A_L}$ but insensitive to L_L (Figure 6d). Local sensitivity of the saltwater wedge area to L_T (result not presented for the sake of brevity) indicates that when this parameter is increased, the saltwater wedge extends landward at the saltwater toe, but withdraws seaward at the top of the saltwater wedge, causing the total area of the saltwater wedge to remain almost constant. The increase of L_{pot} is mainly controlled by $\overline{A_L}$ but it is more affected by the variability of $\overline{A_T}$ than that of $\overline{A_L}$. $\overline{A_T}$ is also a significant controlling parameter for L_{pot} (Figure 6e).

The impact of parameters on the SWI metrics is investigated considering their marginal effects, as calculated in Appendix C. "Marginal effect" represents the evolution of a metric with respect to a given parameter while considering all other parameters as constant, at their average values within their ranges of variability.

Here, the focus is on the impact of the dependency of these parameter values on the flow direction. This dependency can be measured using the parameters L_L and L_T. In Figure 7, the marginal effects of a particular range of these parameters on the SWI metrics are investigated. Figures 7a and 7b show that L_{toe} generally increases with the increase in L_L and L_T. In contrast, an increase of L_L and L_T leads to a sharper mixing zone (Figures 7c and 7d). Q_t increases with the increase of L_L (Figure 7e). Different regimes of variation of Q_t with respect to L_T can be observed in Figure 7f. The variation of A_F with respect to L_L exhibits two regimes: it decreases when L_L is <0.25 and increases otherwise (Figure 7g). A_F increases with L_T (Figure 7h). L_{pot} increases with the increase in L_L and L_T (Figures 7i and 7j).

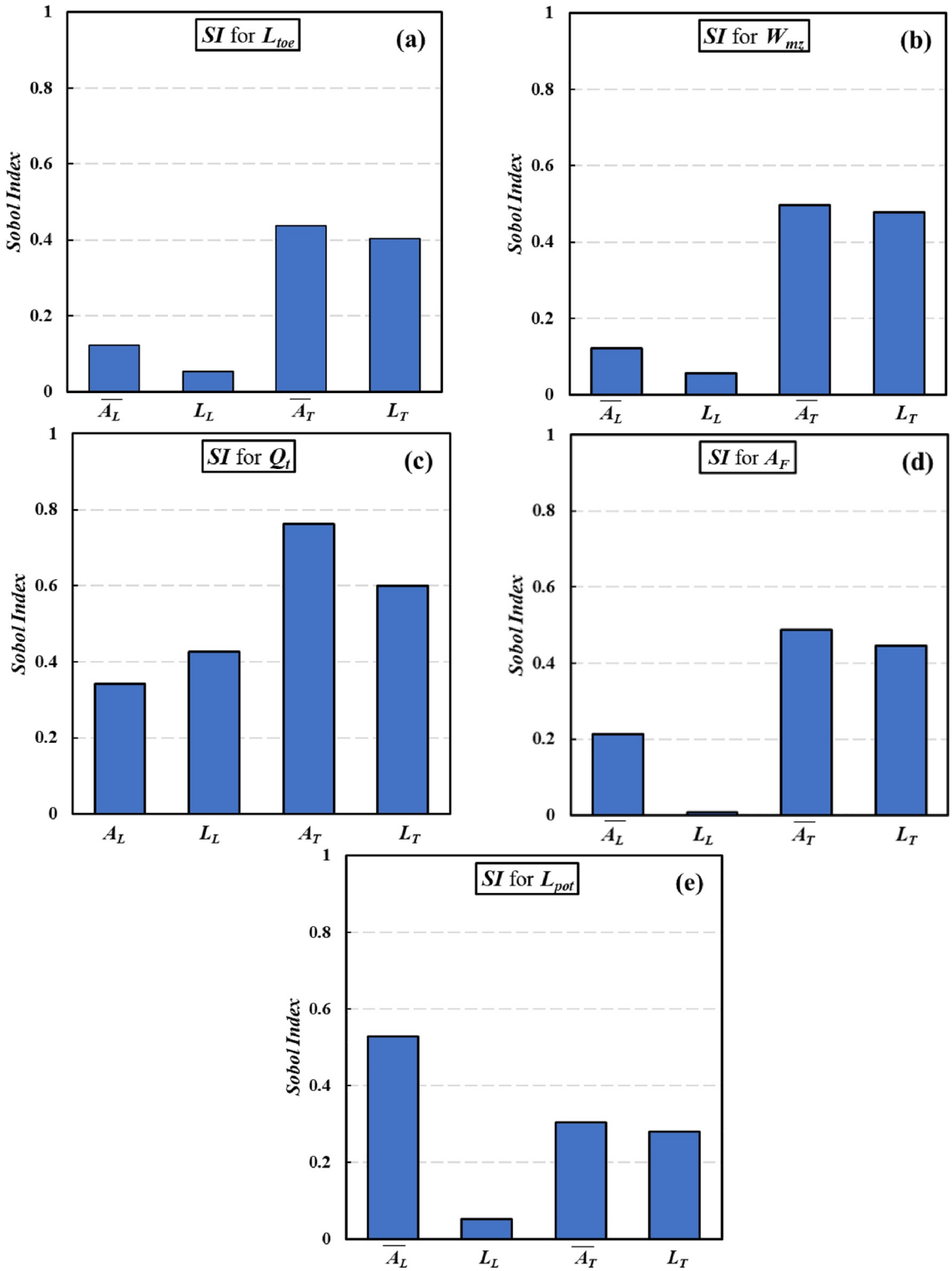

Figure 6. The total Sobol' indices (SIs) (S_i^T) representing the sensitivity of (a) L_{toe}, (b) W_{mz}, (c) Q_t, (d) A_F, and (e) L_{pot} to the flow-direction-dependent (FDD) dispersivity parameters.

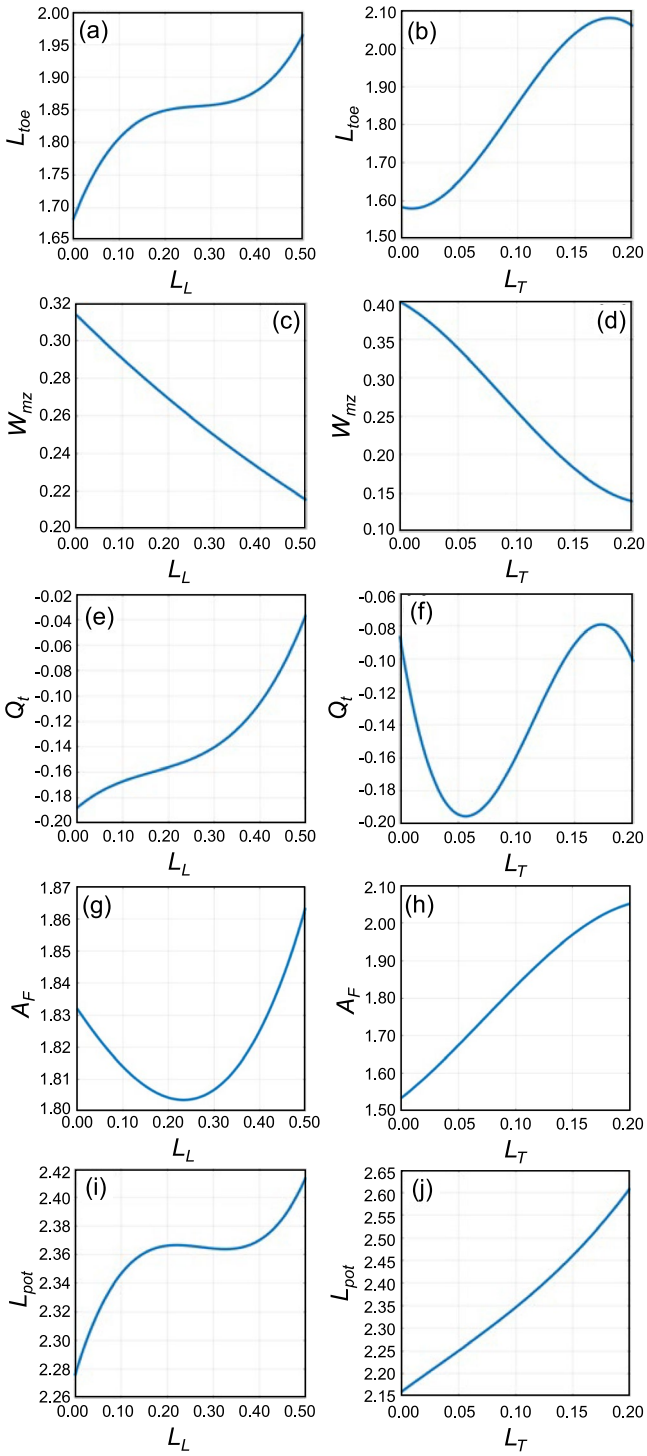

Figure 7. Marginal effects of the flow dependency of dispersivity (L_L and L_T) on the seawater intrusion (SWI) metrics.

5. FDD Versus FDI Dispersivities at Field Scale and Under Dynamic Conditions: The Akkar CA in Lebanon

The HP allows for investigating the impacts of FDD dispersivities on SWI under a steady-state regime without pumping. To investigate the effects of FDD dispersivities under more realistic and dynamic conditions, in heterogeneous domains and at real scale, SWI is considered under conditions of pumping stress and climate change in the CA of the Akkar plain in north Lebanon (Figure 8a). Simulations are carried out with the newly developed version of TRACES that simulates FDD dispersivities, and with the previous version simulating FDI dispersivities. The modeled area comprises a large cultivated coastal plain with cereal crops and market gardens, with high mountains to the east, in the most rural region of Lebanon. Groundwater is the primary source of freshwater used for irrigation and for domestic water supply. The Akkar plain has experienced a rapid population growth (7.4% between 2007 and 2012). Overexploitation of groundwater has resulted in SWI and the salinization of some pumping wells, and salinization has been exacerbated due to recent reductions in precipitation recharge that may be due to long-term climate change. Further, the demand for freshwater in the region has recently increased because of a massive migration of Syrian refugees to the Akkar District. Thus, there is a high risk of further aquifer contamination by SWI if active management strategies are not implemented as soon as possible.

The Akkar model is developed as a 2D shore-perpendicular cross-section, shown in Figure 8b, considering the saturated zone below sea level. The 2D cross-section extends 6 km onshore and 2 km offshore. The offshore vertical boundary is located 2 km from the coast in order to minimize the impact of this arbitrary vertical boundary location on the aquifer salinity distribution. The third dimension (perpendicular to the plane of the cross-section) is 1 km.

Figure 8b shows the domain geometry and dimensions as well as the corresponding hydrogeology. The hydrogeological units within the Akkar basin in its middle section consist of yellowish limestone and sandstone (Zone 6), overlain by a layer of recent alluvial and fluvial deposits of quaternary age with different hydraulic parameters (Zones 1, 2, 3, 4, 5), including a distinct section composed of fine sand and gravel (Zone 4) (United Nations Development Program, 2014). The top of the "impermeable" bottom layer, composed of low-permeability marls, occurs at depths ranging from 80 to 100 m. The hydraulic characteristics of these geological units are given in Table 2. The hydraulic conductivities used for the simulations are obtained from a numerical flow model (GMS MODFLOW), which was calibrated against water levels observed in the Akkar plain (United Nations Development Program, 2014).

All flow boundary conditions are schematized and shown in Figure 8b. The offshore vertical and sea-bottom boundaries are modeled with Dirichlet pressure boundary conditions, having a hydrostatic pressure based on the seawater density and depth of seawater. Where seawater enters the aquifer along these offshore boundaries, the total dissolved solids (TDS) concentration of inflowing water is set to 39 g/L. At the landward vertical boundary, a constant influx is applied, representative of the relatively weak regional groundwater flow. The total influx at this boundary is set to 6×10^{-6} (m^3/d) for the full 1-km width of the modeled cross-section. Seawater does not reach the vertical inland boundary; thus, without over-constraining the model setup, zero salinity concentration is imposed there to simulate freshwater influx. Recharge is simulated as an imposed flux on the onshore domain top surface. Observed recharge from 1962 to 2020 and projections for

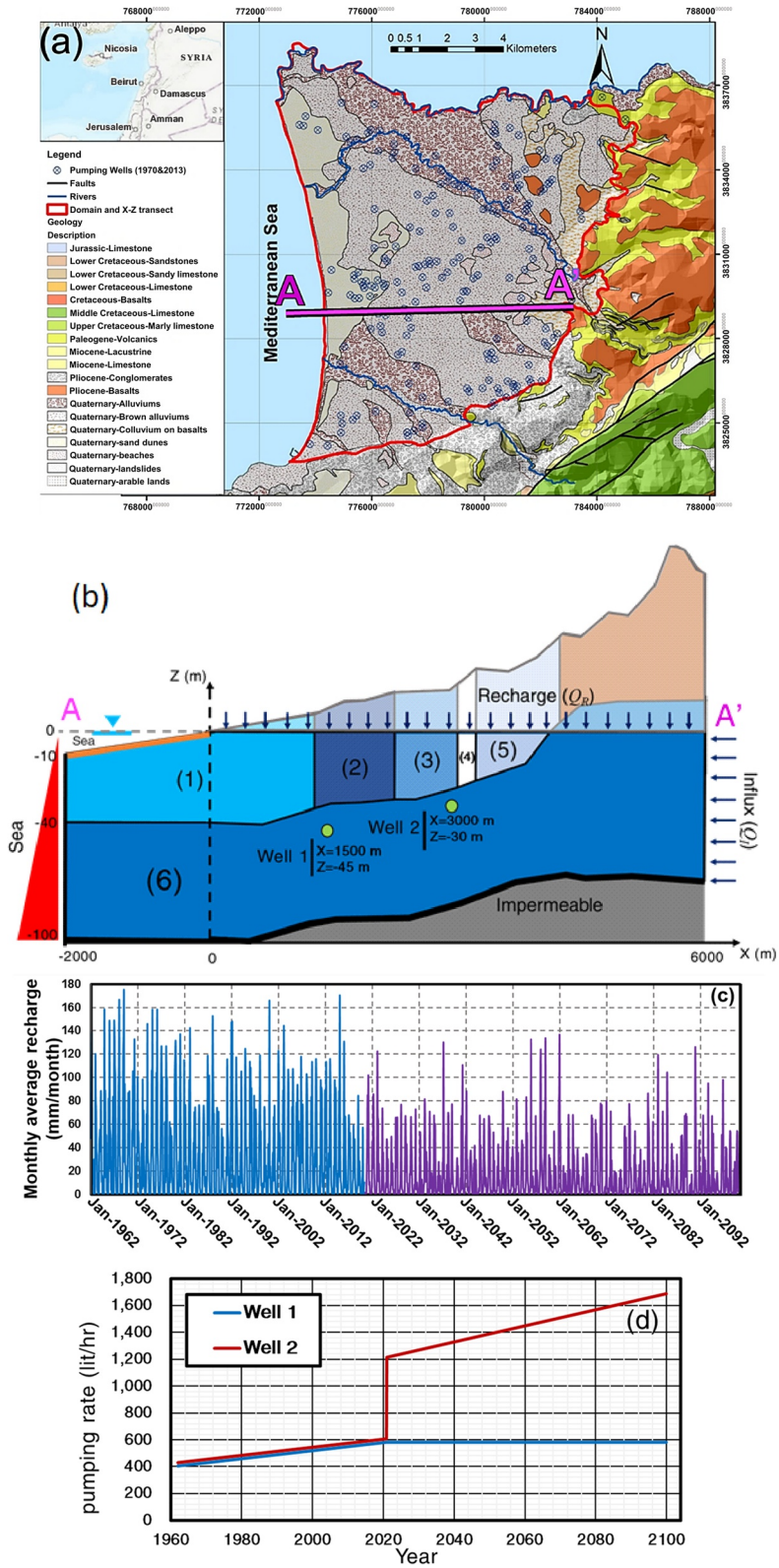

Figure 8. Representation of: (a) the location of the Akkar plain aquifer in north Lebanon, (b) vertical cross-section schematic used to simulate seawater intrusion (SWI) with aquifer geology and boundary conditions (the orange zone at the sea bottom represents a 2-m sediment layer), (c) the monthly average recharge with real data until the end of 2020 and projections under climate change stresses from 2020 to 2099, and (d) pumping rates in production wells.

a future climate scenario are given in Figure 8c (downscaled data from the IPSL_CM5 Global Climate Model (GCM) with Representative Concentration Pathway (RCP) 6.0 scenario; Van Vuuren et al., 2011).

Hundreds of wells are randomly located within the coastal plain, as can be seen in Figure 8a. For the 2D assumption, the pumping rate used for the 2D cross-section is calculated by dividing the total pumping rate of all wells by the width of this cross-section (1 km). In comparison with three-dimensional (3D) simulation, a 2D cross-sectional simulation generally reduces the simulated amount of drawdown and saltwater upconing at any particular well because simulated withdrawal is spread over the entire width of the cross-section and hydraulic heads cannot change in lateral directions from a well in the missing third dimension. Despite this approximation, a 2D analysis is extremely useful because it provides an effective means of evaluating the overall aquifer system dynamics and it also provides an evaluation of the danger of SWI to pumping at any distance from the coast at which a well is located in the 2D model. The 2D analysis provides and initial assessment of system dynamics and vulnerabilities, and 3D simulation can later be used to evaluate more details of these aspects.

To evaluate the possibility of seawater contamination of wells at two distances from the coast, two (two-dimensional) wells are included in the model to represent pumping in the aquifer (see Figure 8b). The first well is located near the sea (1.5 km onshore) at 45 m below sea level, while the second one is located further inland (3 km onshore) at 30 m below the sea level. The two designated wells have pumping rates of 0.15 and 0.01 $m^3\ s^{-1}$, respectively, as recorded in 1969 (FAO). These pumping rates are calculated by dividing the total pumping rate of all wells by the width of this cross-section. Pumping rates with real data from 1962 to 2020 and projections under increasing water demand scenarios up to 2099 are given in Figure 8d. The projected pumping rates are based on a yearly increase in water consumption of about 0.33% calculated on the basis of increased well abstraction from 1970 till 2013 (United Nations Development Program, 2014).

In the FDD model, the average dispersivities are assumed to be 50.25 m for $\overline{\alpha_L}$ and 0.55 m for $\overline{\alpha_T}$. l_L and l_T are assumed to be, respectively, 99.5 and 0.9 m. The equivalent dispersivity values ($\alpha_L^{\max} = 100\text{m}, \alpha_L^{\min} = 1\text{m}, \alpha_T^{\max} = 1\text{m}, \alpha_L^{\min} = 0.1\text{m}$) are consistent with the aquifer scales (Yu & Michael, 2019) and are reasonable for the hydrogeologic fabric of this aquifer system. Simulations with the FDI model are performed by setting $l_L = l_T = 0$. Thus, the same average dispersivity values are used in the FDD and FDI models, allowing direct comparison of their results and any differences will be due to only the direction-dependence of the dispersivities. A computational mesh of about 60,000 triangular elements is used. Groundwater pumping in the Akkar aquifer began in 1962 (FAO, 1970). Simulations are performed for three periods, described below.

Period 1: The models are first run without pumping until reaching a steady-state predevelopment salinity distribution, representing the natural equilibrium between fresh and saline waters before 1962. For these prepumping simulations, recharge is held constant, equivalent to the average observed recharge in 1962 (90 mm $year^{-1}$). Resultant steady-state simulated salinity distributions are shown in Figures 9a and 9b for FDI and FDD models, respectively. Due to significant recharge and lack of pumping, the steady-state saltwater wedge is located relatively close to the sea.

The saltwater wedge intrudes farther inland with the FDD model but the FDD potable water area is greater. The mixing zone with the FDI model is wider than that with the FDD model. This results from the fact that in this discharge zone, the vertical component of groundwater flow is significant. In the FDD model, the longitudinal dispersivity in this area thus has its minimum value, whereas it has the higher average value in the FDI model.

Period 2: The second simulation period extends from 1962 to 2020. It is performed by including pumping in both wells (1 and 2) with observed recharge and pumping rates (see Figures 8c and 8d). Monthly average recharge values are used in these simulations. The transient results in 2020 with FDI and FDD models are shown in Figures 9c and 9d, respectively. These figures show that SWI into the aquifer occurs due to pumping and well (1) is impacted, whereas well (2) is not affected by SWI. The time variation of salinity at the observation point in well (1) is shown in Figure 10a. The FDI model predicts lower salinity than the FDD model, because the FDI model exaggerates the mixing processes, thus underestimating seawater penetration into the aquifer. This agrees with the results in Abarca et al. (2007) and Fahs et al. (2016), which show that greater diffusion processes lead to less SWI. In 2020, the FDD model predicts a dimensionless concentration of 0.013 in well (1), corresponding to a salinity (TDS concentration) of about 0.51 g/L, which is equivalent to the salinity currently observed in the aquifer at around 1.5 km from the coast. Recent observations in some wells around 1.5 km from the coast indicate

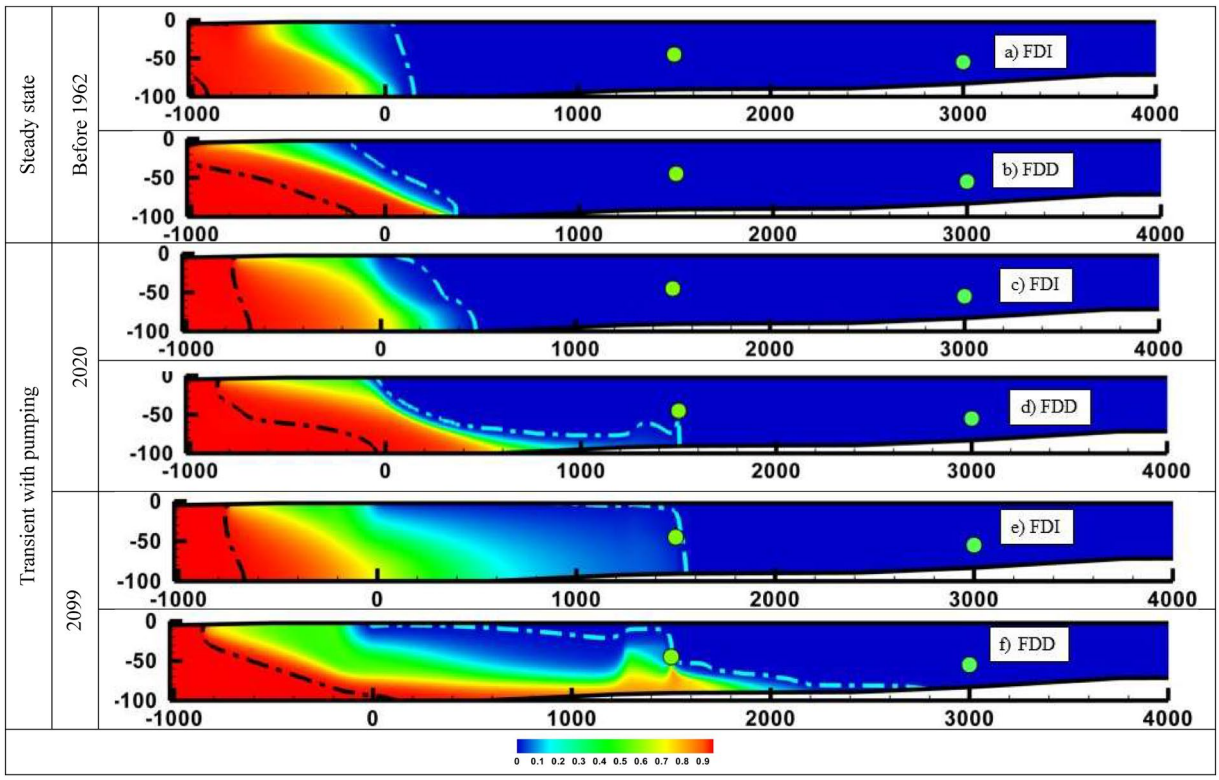

Figure 9. Salinity distribution in the Akkar aquifer before 1962 (top), currently at 2020 (middle), and predictions at 2099 (bottom) with the flow-direction-independent (FDI; a, c and e) and flow-direction-dependent (FDD; b, d and f) models. The black line represents the 0.99 isohyet while the blue line represents the limit of potability (0.01 isohyet). The green points indicate the pumping well locations.

a salinity of about 0.6 g/L (TDS). The FDI model underestimates the current salinity, simulating a dimensionless concentration of about 0.001 that corresponds to almost freshwater.

Figures 10d–10f show the time variation of L_{toe}, L_{pot}, and A_F for the period 1962–2020. In this case, A_F represents the ratio of the onshore freshwater area to the total area of the onshore domain. Figures 10d and 10e show that L_{toe} and L_{pot} calculated with the FDD model are greater than that with the FDI model. For A_F, both models lead to equivalent results before 2020 (Figure 10f). This is due to the fact that the FDI model causes more dispersive mixing of freshwater and seawater that reduces bulk intrusion, while the FDD model predicts a narrower mixing zone and a more-intruded saltwater wedge.

Period 3: The third simulation period, 2020–2099, forecasts SWI in the aquifer under climate change stresses and with over-pumping induced by increasing water demand. The generally lower average monthly recharge (than for the previous period), presented in Figure 8c, is used in these simulations. Groundwater pumping is assumed to increase linearly, as shown in Figure 8d. The predicted salinity distributions in the aquifer with FDD and FDI models are shown in Figures 9e and 9f, respectively. The discrepancy between the two model forecasts is more significant than in the earlier periods, and the FDD model predicts that well (2) will be impacted. As in the previous cases, the FDI model causes more mixing than the FDD model, and predicts no impact on the potability of water pumped from well (2). The FDI model predicts less SWI than the FDD model. The time variation of the concentration at wells (1) and (2) is plotted in Figures 10b and 10c, respectively. The FDD model shows that SWI is predicted to rapidly increase the salinity (TDS concentration) near well (1), reaching >5.850 g/L (~15% seawater), in 2099. The FDI model indicates that TDS concentration will remain <0.66 g/L, which is almost equivalent to the potable water limit (0.6 g/L). The FDD model also predicts that SWI will begin to affect the salinity in well (2) within about 70 years (at around 2090). By 2099, the TDS concentration in well (2) is predicted to be about 0.24 g/L. In contrast, the FDI model predicts that no groundwater salinity will reach well (2).

There is a significant discrepancy between the models regarding the predictions for 2099 and the practical conclusions. The FDI model indicates that the current trajectory and management approach will affect the salinity

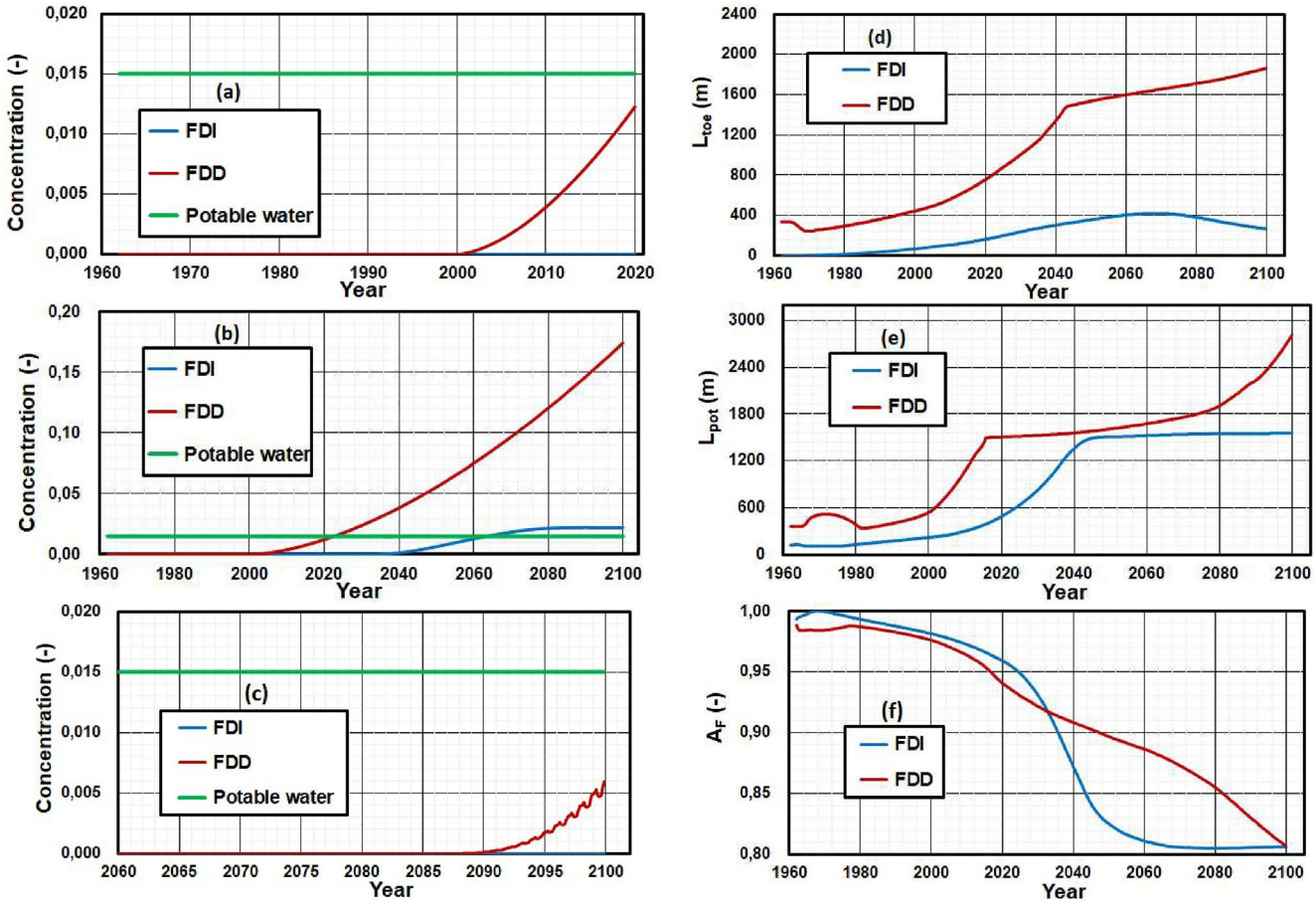

Figure 10. Time variation of the relative concentration (c/C_s) in well (1) (a from 1960 to 2020 and b from 1960 to 2100), the relative concentration in well (2) (c), L_{toe} (d), L_{pot} (e), and A_F (f). A_F represents the ratio of the he freshwater area to the total area of the domain (excluding the offshore part).

neither at 1.5 km nor at 3 km from the coast. This is completely different from the results of the FDD model, which show that, with the current strategies for groundwater pumping and with the assumed climate change, the water at 1.5 km from the coast will have become salinized and unusable. Also, increasing salinity will be observed in well (2) in few decades. Moreover, Figures 9d and 9e show clearly that the FDI model predicts a smaller intrusion of the saltwater wedge within the aquifer than does the FDD model. However, for the total area of the freshwater zone, both models indicate equivalent results before 2020 (Figure 10f). This is due to the fact that the FDI model causes more dispersive mixing of freshwater and seawater, while the FDD model leads to a narrower mixing zone but to a more-intruded saltwater wedge. After 2020, the total predicted area of the freshwater zone for the FDI model is less than that predicted by the FDD model.

6. Conclusions

In variable-density-flow simulation models, constant-dispersivity coefficients are commonly used to represent longitudinal and transverse dispersion. However, in CAs, due to the difference between horizontal and vertical scales and due to the structure of the hydrogeologic fabric of the aquifer, constant-dispersivity coefficients do not capture the primary processes of dispersion that actually occur.

Velocity variability that causes mechanical dispersion depends on which direction the flow occurs, relative to the seaward versus vertical extent of the aquifer, and relative to the structural direction of heterogeneities in the aquifer fabric. Thus, dispersivity coefficients must depend on the direction of flow through the aquifer fabric. This gives rise to the definition of FDD dispersivity (Voss, 1984; Voss & Provost, 2002), which impacts the simulated SWI process and the resultant forecast quality of groundwater.

Contrasting simulations of the classical Henry SWI problem that employ either constant or FDD dispersivity exhibit significant differences in SWI extent and in the forecast region of potable groundwater. SWI is forecast to reach much farther inland by the model based on FDD dispersivities. The HP indicates that these dispersion parameters are the most important controls on SWI and region of potable groundwater under steady-state conditions. A global sensitivity analysis, performed to investigate the effect of dispersion parameters on the saltwater wedge in the HP, indicates that salinity distribution and SWI metrics are more sensitive to the variability of the transverse dispersivity with flow direction than that of the longitudinal dispersivity.

Insight into the impact of FDD dispersivities under nonsteady-state and pumping conditions and in heterogonous domains, is gained by consideration of SWI in a regional CA in north Lebanon (Akkar plain) under climate change and under conditions of changing pumping stress. The discrepancies found between FDI and FDD model forecasts for this real-scale CA are more pronounced than for the HP. The FDI dispersivities model creates larger amounts of dispersion and thus lower variable-density driving forces, leading to less inland SWI than does the FDD dispersivities model. Under conditions of future climate change and increasing pumping, the FDD dispersivities model predicts a high salinity (above the limit of potable water) at >1.5 km from the coast, whereas the constant dispersivities model predicts low salinity.

These significantly different forecasts of SWI and potable groundwater zone in the aquifer would imply very different management strategies for many CAs. Use of the wrong representation of dispersion will negatively impact the efficacy of CA management strategies that are based on model results. Thus, this work suggests that further investigations concerning the use of FDD dispersivities in simulations of SWI in CAs is warranted. Neglecting the dependency of the dispersivities on the flow direction in aquifers may have a significant impact on the correctness of predictive results of the variable-density groundwater flow models that are used to evaluate SWI.

Appendix A: List of Acronyms

List of acronyms used in the text:

FDD	Flow-direction-dependent
FDI	Flow-direction-independent
CA	Coastal aquifer
SWI	Seawater intrusion
HP	Henry problem
SIM	Sharp-interface model
VDF	Variable-density flow
SA	Semianalytical
PCE	Polynomial Chaos Expansion
SI	Sobol' indices
TRACES	Transport of RadioACtive Elements in Subsurface—in-house code

Appendix B: Nondimensional System and SA Solution

The dimensionless equations of the VDF model are usually obtained by assuming that buoyancy as the primary force (Guevara Morel et al., 2015). For HP, the dimensionless equations are derived using the advection as primary force. As in Fahs et al. (2018), the stream function form of the governing equations is

$$\frac{r_K}{NG}\left(\frac{\partial^2\Psi}{\partial Z^2}+\frac{\partial^2\Psi}{\partial X^2}\right)-\frac{\partial C}{\partial X}-\frac{1}{\xi}=0 \tag{B1}$$

$$\begin{aligned} &b_m\left(\frac{\partial^2 C}{\partial X^2}+\frac{\partial^2 C}{\partial Z^2}\right)-\frac{\partial\Psi}{\partial Z}\frac{\partial C}{\partial X}+\frac{\partial\Psi}{\partial X}\frac{\partial C}{\partial Z}-\frac{1}{\xi}\frac{\partial\Psi}{\partial Z}-\frac{\partial C}{\partial X}-\frac{1}{\xi}+\Delta_{1,1}\frac{\partial^2 C}{\partial X^2}\\ &+2\Delta_{1,2}\frac{\partial^2 C}{\partial X\partial Z}+\Delta_{2,2}\frac{\partial^2 C}{\partial Z^2}+\left(\frac{\partial C}{\partial X}+\frac{1}{\xi}\right)\left(\frac{\partial\Delta_{1,1}}{\partial X}+\frac{\partial\Delta_{1,2}}{\partial Z}\right)+\frac{\partial C}{\partial Z}\left(\frac{\partial\Delta_{1,2}}{\partial X}+\frac{\partial\Delta_{2,2}}{\partial Z}\right)=0 \end{aligned} \tag{B2}$$

where $X(=x/d)$ and $Z(=z/d)$ are the dimensionless coordinates, $\Psi=(\psi/q_d-Z)$ is the shifted dimensionless stream function (ψ is the stream function), $C=(c-X/\xi)$ is the shifted concentration, $\xi(=\ell/d)$ is the aspect ratio of the domain. r_k, NG, b_m are dimensionless numbers governing the flow and transport process and are expressed as follows:

$$r_k=\frac{k_z}{k_x} \tag{B3}$$

$$NG=\frac{k_z g\,(\rho_1-\rho_0)}{\mu q_d} \tag{B4}$$

$$b_m=\frac{\varepsilon D_m}{q_d} \tag{B5}$$

where $k_x\left[L^2\right]$ and $k_z\left[L^2\right]$ are, respectively, permeability in x and z directions.

The dimensionless dispersion tensor ($\Delta_{i,j}=D_{i,j}/q_d$) can be expressed as follows:

$$\Delta_{1,1}=\frac{A_L Q_x^2+A_T Q_z^2}{|\mathbf{Q}|} \tag{B6}$$

$$\Delta_{2,2}=\Delta_{1,1}=\frac{A_L Q_z^2+A_T Q_x^2}{|\mathbf{Q}|} \tag{B7}$$

$$\Delta_{1,2}=\Delta_{2,1}=(A_L-A_T)\frac{Q_x Q_z}{|\mathbf{Q}|} \tag{B8}$$

where $A_L\,(=\alpha_L/d)$ and $A_T\,(=\alpha_T/d)$ are the FDD dimensionless dispersivities, $\mathbf{Q}\,(=q.d/q_d)$ is the dimensionless velocity field and Q_x and Q_z are the horizontal and vertical velocity components.

A_L and A_T can be expressed as follows:

$$A_L=\frac{|\mathbf{Q}|^2 A_L^{\max}A_L^{\min}}{A_L^{\min}{Q_x}^2+A_L^{\max}{Q_z}^2} \tag{B9}$$

$$A_T=\frac{|\mathbf{Q}|^2 A_T^{\max}A_T^{\min}}{A_T^{\min}{Q_z}^2+A_T^{\max}{Q_x}^2} \tag{B10}$$

where $A_L^{\max}\left(=\alpha_L^{\max}/d\right)$ and $A_L^{\min}\left(=\alpha_L^{\min}/d\right)$ are the maximum and minimum longitudinal dispersivities and $A_T^{\max}\left(=\alpha_T^{\max}/d\right)$ and $A_T^{\min}=\left(\alpha_T^{\min}/d\right)$ are the maximum and minimum transverse dispersivities.

As discussed in the previous section, the average values and the range of variability of the nondimensional dispersivities are used as primary parameters in our analysis. Thus, we defined the following parameters:

$$\begin{aligned}\overline{A_L}&=\frac{\overline{\alpha_L}}{d}=\frac{A_L^{\min}+A_L^{\max}}{2}\\ \overline{A_T}&=\frac{\overline{\alpha_T}}{d}=\frac{A_T^{\min}+A_T^{\max}}{2}\\ L_L&=\frac{l_L}{d}=A_L^{\max}-A_L^{\min}\\ L_T&=\frac{l_T}{d}=A_T^{\max}-A_T^{\min}\end{aligned} \tag{B11}$$

The system of Equations B1 and B2 is solved using the Fourier-Galerkin method. Thus, the unknowns Ψ and C are expanded into Fourier series that satisfy the periodic boundary conditions

$$\Psi=\sum_{m=1}^{Nm}\sum_{n=0}^{Nn}A_{m,n}\sin(m\pi Z)\cos\left(n\pi\frac{X}{\xi}\right) \tag{B12}$$

$$C=\sum_{r=0}^{Nr}\sum_{s=1}^{Ns}B_{r,s}\cos(r\pi Z)\sin\left(s\pi\frac{X}{\xi}\right) \tag{B13}$$

where Nm, Nn, Nr, and Ns are the truncation orders for the Fourier series and $A_{m,n}$ and $B_{r,s}$ are the Fourier series coefficients.

Appendix C: Global Sensitivity Analysis Method

To construct the sparse PCE for the SWI metrics, we denote each scalar metric with y, and write the vector of input variable parameters as $\mathbf{x} = (x_1, x_2, \ldots, x_n)$. Herein all the input parameters are assumed independent and uniformly distributed over the unit hypercube K^n. Thus, the input-output relationship of the SWI model can be approximated by the PCE truncated in a given order d

$$y \approx M(\mathbf{x}) = \sum_{\mathbf{b}\in A^{d,n}} a_{\mathbf{b}}\varphi_{\mathbf{b}}(\mathbf{x}) \text{ with } \varphi_{\mathbf{b}}(\mathbf{x}) = \varphi_{b_1\ldots b_n}(\mathbf{x}) = \prod_{i=1}^{n} \varphi_{b_i}(x_i) \tag{C1}$$

where $\varphi_{\mathbf{b}}(\mathbf{x})$ is a multidimensional polynomial given by the tensor product of univariate orthonormal shift-Legendre polynomials, $a_{\mathbf{b}}$ is the coefficient of the polynomial, $\mathbf{b} = b_1 \ldots b_n$ $(b_i \in \mathrm{N},\ 1 \le i \le n)$ is an n-dimensional index belonging to the set $A^{d,n} = \{\mathbf{b} \in N^n : |\mathbf{b}| \le d\}$, and b_i represents the degree of the univariate polynomial $\varphi_{b_i}(x_i)$. Thus, the total degree of the polynomial term $\varphi_{\mathbf{b}}(\mathbf{x})$ satisfies $|\mathbf{b}| = \sum_{i=1}^{b} b_i \le d$. To prevent possible computational issues such as overfitting and curse of dimensionality, the Kashyap information criterion based on the Bayesian model averaging is adopted to construct a sparse representation of the PCE model such that $y \approx M_A(\mathbf{x}) = \sum_{\mathbf{b}\in A} a_{\mathbf{b}}\varphi_{\mathbf{b}}(\mathbf{x})$ with $A \subseteq A^{d,n}$, where $\mathrm{card}(A) \ll \mathrm{card}\left(A^{d,n}\right)$ and the operator "card" provides the cardinality of a set.

The effect of the uncertain input parameters on the SWI metrics is measured via the variance-based sensitivity indices of Sobol'. The sth-order sensitivity indices due to the interaction effect of the input variables $\left\{x_{i_1}, \ldots, x_{i_s}\right\}$ are easily estimated from the polynomial coefficients of the sparse PCE representation as follows:

$$S_{i_1\ldots i_s} = \frac{\sum_{\mathbf{b}\in I_{i_1\ldots i_s}} a_{\mathbf{b}}^2}{\sum_{\mathbf{b}\in A\setminus\{\mathbf{0}\}} a_{\mathbf{b}}^2} \tag{C2}$$

where

$$I_{i_1\ldots i_s} = \left\{\mathbf{b} \in A : \begin{array}{c} b_k > 0,\ k \in (i_1, \ldots, i_s) \\ b_k = 0,\ k \notin (i_1, \ldots, i_s) \end{array}, \forall k = 1, \ldots, n\right\} \tag{C3}$$

The numerator in Equation C2 denotes the partial variance of y due to the sth-order interaction of the input variables $\left\{x_{i_1}, \ldots, x_{i_s}\right\}$, while the denominator represents the total variance of y. In specific, the first-order Sobol' index S_i, which measures the influence due to the parameter x_i alone, and the total order SI S_i^T that summarizes the overall contribution of the input variable x_i by taking into account its marginal and interactive effects can be derived from Equation C2

$$S_i = \frac{\sum_{\mathbf{b}\in I_i} a_{\mathbf{b}}^2}{\sum_{\mathbf{b}\in A\setminus\{\mathbf{0}\}} a_{\mathbf{b}}^2} \text{ and } S_i^T = \sum_{\mathbf{b}:\, b_i>0} S_{\mathbf{b}} \tag{C4}$$

The marginal effect of the input parameter x_i is calculated by

$$\int_{K^{n-1}} M_A(\mathbf{x}) d\mathbf{x}_{\sim i} = a_0 + \sum_{\mathbf{b}\in \mathbf{I_i}} a_{\mathbf{b}}\varphi_{\mathbf{b}}(x_i) \tag{C5}$$

where $\int_{K^{n-1}} dx_{\sim i}$ computes the integral of a function over all variables except x_i.

Appendix D: Reference Data for Code Validation

This appendix provides numeric data for concentration, velocity field, and dispersivity coefficients. These data can be used for benchmarking purposes. In the tables A_L ($= \alpha_L/d$) and A_T ($= \alpha_T/d$) are the FDD dimensionless dispersivities, $\mathbf{Q}$ ($= q.d/q_d$) is the dimensionless velocity field and Q_x and Q_z are the horizontal and vertical velocity components (Tables D1 and D2).

Table D1
Information Defining the 0.01, 0.5, and 0.99 Isohyets for the Verification Test Case: Points Coordinates (X and Z), Concentration (C), Nondimensional Velocity Components (Q_x and Q_z), and Longitudinal and Transverse Dispersivities (A_L and A_T)

X	Z	C	Q_x	Q_z	A_L	A_T
1.619	0.099	0.010	0.736	0.259	0.050	0.011
1.719	0.198	0.010	0.907	0.327	0.049	0.011
1.844	0.298	0.010	1.033	0.358	0.051	0.011
2.002	0.402	0.010	1.162	0.394	0.052	0.011
2.160	0.502	0.010	1.308	0.437	0.052	0.011
2.331	0.602	0.010	1.504	0.503	0.052	0.011
2.489	0.701	0.010	1.778	0.589	0.053	0.011
2.626	0.801	0.010	2.191	0.680	0.056	0.011
2.613	0.901	0.010	2.386	0.388	0.081	0.010
2.934	0.901	0.500	4.041	0.829	0.073	0.010
2.938	0.801	0.500	2.621	0.973	0.048	0.011
2.929	0.701	0.500	1.376	1.018	0.024	0.015
2.863	0.602	0.500	0.817	0.775	0.019	0.017
2.726	0.502	0.500	0.725	0.543	0.024	0.015
2.568	0.402	0.500	0.600	0.385	0.028	0.014
2.364	0.298	0.500	0.502	0.281	0.032	0.013
2.152	0.198	0.500	0.371	0.197	0.034	0.012
1.906	0.099	0.500	0.223	0.130	0.030	0.013
2.468	0.099	0.990	−0.251	−0.005	0.100	0.010
2.655	0.198	0.990	−0.232	0.000	0.100	0.010
2.800	0.298	0.990	−0.223	0.010	0.098	0.010
2.909	0.402	0.990	−0.217	0.022	0.092	0.010
2.975	0.502	0.990	−0.205	0.026	0.087	0.010

Table D2
SWI Metrics for the Verification Test Case: Length of the Saltwater Toe (L_{toe}), Length of Potable Water Threshold (L_{pot}), Width of the Mixing Zone (W_{mz}), Total Dimensionless Flux of Saltwater (Q_t), and Dimensionless Salinized Area (A_s)

L_{toe}	1.33
L_{pot}	1.45
W_{mz}	0.27
Q_t	1.12
A_s	0.85

Data Availability Statement

There are no data used in this modeling study.

Acknowledgments
Marwan Fahs acknowledges support from the National School of Water and Environmental Engineering of Strasbourg, University of Strasbourg, through research project PORO6100.

References

Abarca, E., Carrera, J., Sánchez-Vila, X., & Dentz, M. (2007). Anisotropic dispersive Henry problem. *Advances in Water Resources*, *30*(4), 913–926. https://doi.org/10.1016/j.advwatres.2006.08.005

Abdoulhalik, A., & Ahmed, A. A. (2017). How does layered heterogeneity affect the ability of subsurface dams to clean up coastal aquifers contaminated with seawater intrusion? *Journal of Hydrology*, *553*, 708–721. https://doi.org/10.1016/j.jhydrol.2017.08.044

Bouzaglou, V., Crestani, E., Salandin, P., Gloaguen, E., & Camporese, M. (2018). Ensemble Kalman filter assimilation of ERT data for numerical modeling of seawater intrusion in a laboratory experiment. *Water*, *10*(4), 397. https://doi.org/10.3390/w10040397

Chang, Q., Zheng, T., Zheng, X., Zhang, B., Sun, Q., & Walther, M. (2019). Effect of subsurface dams on saltwater intrusion and fresh groundwater discharge. *Journal of Hydrology*, *576*, 508–519. https://doi.org/10.1016/j.jhydrol.2019.06.060

de Dreuzy, J.-R., Carrera, J., Dentz, M., & Le Borgne, T. (2012). Asymptotic dispersion for two-dimensional highly heterogeneous permeability fields under temporally fluctuating flow. *Water Resources Research*, *48*, W01532. https://doi.org/10.1029/2011WR011129

Dell'Oca, A., Riva, M., Carrera, J., & Guadagnini, A. (2018). Solute dispersion for stable density-driven flow in randomly heterogeneous porous media. *Advances in Water Resources*, *111*, 329–345. https://doi.org/10.1016/j.advwatres.2017.10.040

Dentz, M., Comolli, A., Hakoun, V., & Hidalgo, J. J. (2020). Transport upscaling in highly heterogeneous aquifers and the prediction of tracer dispersion at the MADE site. *Geophysical Research Letters*, *47*, e2020GL088292. https://doi.org/10.1029/2020GL088292

Dentz, M., Tartakovsky, D. M., Abarca, E., Guadagnini, A., Sanchez-Vila, X., & Carrera, J. (2006). Variable-density flow in porous media. *Journal of Fluid Mechanics*, *561*, 209. https://doi.org/10.1017/S0022112006000668

Diersch, H.-J. G. (2014). *FEFLOW*. Springer. https://doi.org/10.1007/978-3-642-38739-5

Fahs, M., Ataie-Ashtiani, B., Younes, A., Simmons, C. T., & Ackerer, P. (2016). The Henry problem: New semianalytical solution for velocity-dependent dispersion. *Water Resources Research*, *52*, 7382–7407. https://doi.org/10.1002/2016WR019288

Fahs, M., Koohbor, B., Belfort, B., Ataie-Ashtiani, B., Simmons, C., Younes, A., & Ackerer, P. (2018). A generalized semi-analytical solution for the dispersive henry problem: Effect of stratification and anisotropy on seawater intrusion. *Water*, *10*(2), 230. https://doi.org/10.3390/w10020230

Fajraoui, N., Fahs, M., Younes, A., & Sudret, B. (2017). Analyzing natural convection in porous enclosure with polynomial chaos expansions: Effect of thermal dispersion, anisotropic permeability and heterogeneity. *International Journal of Heat and Mass Transfer*, *115*, 205–224. https://doi.org/10.1016/j.ijheatmasstransfer.2017.07.003

FAO. (1970). *Projet de Développement Hydro-Agricole: Etude Hydrogeologique De La Plaine D'Akkar*. République Libanaise, Ministère des Ressources Hydrauliques et Électriques.

Gelhar, L. W., & Axness, C. L. (1983). Three-dimensional stochastic analysis of macrodispersion in aquifers. *Water Resources Research*, *19*(1), 161–180. https://doi.org/10.1029/WR019i001p00161

Gouze, P., Puyguiraud, A., Porcher, T., & Dentz, M. (2021). Modeling longitudinal dispersion in variable porosity porous media: Control of velocity distribution and microstructures. *Frontiers in Water*, *3*, 766338. https://doi.org/10.3389/frwa.2021.766338

Graf, T., & Therrien, R. (2005). Variable-density groundwater flow and solute transport in porous media containing nonuniform discrete fractures. *Advances in Water Resources*, *28*(12), 1351–1367. https://doi.org/10.1016/j.advwatres.2005.04.011

Graham, M. T., MacAllister, D. J., Vinogradov, J., Jackson, M. D., & Butler, A. P. (2018). Self-potential as a predictor of seawater intrusion in coastal groundwater boreholes. *Water Resources Research*, *54*, 6055–6071. https://doi.org/10.1029/2018WR022972

Guevara Morel, C. R., van Reeuwijk, M., & Graf, T. (2015). Systematic investigation of non-Boussinesq effects in variable-density groundwater flow simulations. *Journal of Contaminant Hydrology*, *183*, 82–98. https://doi.org/10.1016/j.jconhyd.2015.10.004

Held, R., Attinger, S., & Kinzelbach, W. (2005). Homogenization and effective parameters for the Henry problem in heterogeneous formations. *Water Resources Research*, *41*, W11420. https://doi.org/10.1029/2004WR003674

Henry, H. R. (1964). Effects of dispersion on salt encroachment in coastal aquifers. *U.S. Geological Survey Water-Supply Paper*, *1613-C*, 70–84.

Hoteit, H., Ackerer, P. H., & Mosé, R. (2004). Nuclear waste disposal simulations: Couplex test cases. *Computational Geosciences*, *8*(2), 99–124. https://doi.org/10.1023/B:COMG.0000035074.37722.71

Hussain, M. S., Abd-Elhamid, H. F., Javadi, A. A., & Sherif, M. M. (2019). Management of seawater intrusion in coastal aquifers: A review. *Water*, *11*(12), 2467. https://doi.org/10.3390/w11122467

Kalaoun, O., Jazar, M., & Al Bitar, A. (2018). Assessing the contribution of demographic growth, climate change, and the refugee crisis on seawater intrusion in the tripoli aquifer. *Water*, *10*(8), 973. https://doi.org/10.3390/w10080973

Karatzas, G. P., & Dokou, Z. (2015). Optimal management of saltwater intrusion in the coastal aquifer of Malia, Crete (Greece), using particle swarm optimization. *Hydrogeology Journal*, *23*(6), 1181–1194. https://doi.org/10.1007/s10040-015-1286-6

Ketabchi, H., Mahmoodzadeh, D., Ataie-Ashtiani, B., & Simmons, C. T. (2016). Sea-level rise impacts on seawater intrusion in coastal aquifers: Review and integration. *Journal of Hydrology*, *535*, 235–255. https://doi.org/10.1016/j.jhydrol.2016.01.083

Kolditz, O., Bauer, S., Bilke, L., Böttcher, N., Delfs, J. O., Fischer, T., et al. (2012). OpenGeoSys: An open-source initiative for numerical simulation of thermo-hydro-mechanical/chemical (THM/C) processes in porous media. *Environmental Earth Sciences*, *67*(2), 589–599. https://doi.org/10.1007/s12665-012-1546-x

Langevin, C. D., Thorne, D. T., Dausman, A. M., Sukop, M. C., & Guo, W. (2012). *SEAWAT: A computer program for simulation of three-dimensional variable-density ground-water flow and transport*. USGS. Retrieved from https://www.usgs.gov/software/seawat-a-computer-program-simulation-three-dimensional-variable-density-ground-water-flow

Llopis-Albert, C., Merigó, J. M., & Xu, Y. (2016). A coupled stochastic inverse/sharp interface seawater intrusion approach for coastal aquifers under groundwater parameter uncertainty. *Journal of Hydrology*, *540*, 774–783. https://doi.org/10.1016/j.jhydrol.2016.06.065

Lu, C., & Luo, J. (2010). Dynamics of freshwater-seawater mixing zone development in dual-domain formations. *Water Resources Research*, *46*, W11601. https://doi.org/10.1029/2010WR009344

Mehdizadeh, S. S., Ketabchi, H., Ghoroqi, M., & Hasanzadeh, A. K. (2020). Experimental and numerical assessment of saltwater recession in coastal aquifers by constructing check dams. *Journal of Contaminant Hydrology*, *231*, 103637. https://doi.org/10.1016/j.jconhyd.2020.103637

Nick, H. M., Schotting, R., Gutierrez-Neri, M., & Johannsen, K. (2009). Modeling transverse dispersion and variable density flow in porous media. *Transport in Porous Media*, *78*(1), 11–35. https://doi.org/10.1007/s11242-008-9277-x

Provost, A. M., & Voss, C. I. (2019). SUTRA: A model for saturated-unsaturated, variable-density groundwater flow with solute or energy transport—Documentation of generalized boundary conditions, a modified Implementation of specified pressures and concentrations or temperatures, and the lake capability (techniques and methods).

Reilly, T. E. (1990). Simulation of dispersion in layered coastal aquifer systems. *Journal of Hydrology*, *114*(3–4), 211–228. https://doi.org/10.1016/0022-1694(90)90057-5

Ségol, G. (1994). *Classic groundwater simulations: Proving and improving numerical models*. PTR Prentice Hall.

Shao, Q., Fahs, M., Hoteit, H., Carrera, J., Ackerer, P., & Younes, A. (2018). A 3-D semianalytical solution for density-driven flow in porous media. *Water Resources Research*, *54*, 10094–10116. https://doi.org/10.1029/2018WR023583

Shao, Q., Younes, A., Fahs, M., & Mara, T. A. (2017). Bayesian sparse polynomial chaos expansion for global sensitivity analysis. *Computer Methods in Applied Mechanics and Engineering*, *318*, 474–496. https://doi.org/10.1016/j.cma.2017.01.033

Simpson, M. J., & Clement, T. P. (2004). Improving the worthiness of the Henry problem as a benchmark for density-dependent groundwater flow models: Improving the Henry problem. *Water Resources Research*, *40*, W01504. https://doi.org/10.1029/2003WR002199

Strack, O. D. L., Stoeckl, L., Damm, K., Houben, G., Ausk, B. K., & de Lange, W. J. (2016). Reduction of saltwater intrusion by modifying hydraulic conductivity. *Water Resources Research*, *52*, 6978–6988. https://doi.org/10.1002/2016WR019037

United Nations Development Program. (2014). *Assessment of groundwater resources of Lebanon*. Ministry of Energy and Water.

Valdés-Parada, F. J., Lasseux, D., & Bellet, F. (2016). A new formulation of the dispersion tensor in homogeneous porous media. *Advances in Water Resources*, *90*, 70–82. https://doi.org/10.1016/j.advwatres.2016.02.012

van Engelen, J., Verkaik, J., King, J., Nofal, E. R., Bierkens, M. F. P., & Oude Essink, G. H. P. (2019). A three-dimensional palaeohydrogeological reconstruction of the groundwater salinity distribution in the Nile Delta Aquifer. *Hydrology and Earth System Sciences*, *23*(12), 5175–5198. https://doi.org/10.5194/hess-23-5175-2019

Van Vuuren, D., Edmonds, J., Kainuma, M., Riahi, K., Thomson, A., & Hibbard, K. (2011). The representative concentration pathways: An overview. *Climate Change*, *109*, 5–31. https://doi.org/10.1007/s10584-011-0148-z

Voss, C. I. (1984). Sutra—A finite-element simulation model for saturated-unsaturated, fluid-density-dependent ground-water flow with energy transport or chemically-reactive single-species solute transport. U.S. Geological Survey Water-Resources Investigations Report 84-4369. (p. 409).

Voss, C. I., & Provost, A. M. (2002). Sutra: A model for 2D or 3D saturated-unsaturated, variable-density ground-water flow with solute or energy transport. (Version 2.2, 2010). U.S. Geological Survey Water-Resources Investigations Report 02-4231. (p. 250). https://doi.org/10.3133/wri024231

Voss, C. I., & Provost, A. M. (2010). *SUTRA: A model for saturated-unsaturated, variable-density ground-water flow with solute or energy transport, water-resources investigations Report 02-4231*. U.S. Geological Survey.

Voss, C. I., & Souza, W. R. (1987). Variable density flow and solute transport simulation of regional aquifers containing a narrow freshwater-saltwater transition zone. *Water Resources Research*, *23*(10), 1851–1866. https://doi.org/10.1029/WR023i010p01851z

Werner, A. D., Bakker, M., Post, V. E. A., Vandenbohede, A., Lu, C., Ataie-Ashtiani, B., et al. (2013). Seawater intrusion processes, investigation and management: Recent advances and future challenges. *Advances in Water Resources*, *51*, 3–26. https://doi.org/10.1016/j.advwatres.2012.03.004

Yang, J., Graf, T., Herold, M., & Ptak, T. (2013). Modelling the effects of tides and storm surges on coastal aquifers using a coupled surface-subsurface approach. *Journal of Contaminant Hydrology*, *149*, 61–75. https://doi.org/10.1016/j.jconhyd.2013.03.002

Younes, A., Fahs, M., & Ahmed, S. (2009). Solving density driven flow problems with efficient spatial discretizations and higher-order time integration methods. *Advances in Water Resources*, *32*(3), 340–352. https://doi.org/10.1016/j.advwatres.2008.11.003

Yu, X., & Michael, H. A. (2019). Mechanisms, configuration typology, and vulnerability of pumping-induced seawater intrusion in heterogeneous aquifers. *Advances in Water Resources*, *128*, 117–128. https://doi.org/10.1016/j.advwatres.2019.04.013

Zheng, T., Zheng, X., Sun, Q., Wang, L., & Walther, M. (2020). Insights of variable permeability full-section wall for enhanced control of seawater intrusion and nitrate contamination in unconfined aquifers. *Journal of Hydrology*, *586*, 124831. https://doi.org/10.1016/j.jhydrol.2020.124831